Wind and Structures, Vol. 10, No. 4 (2007) 315-346
DOI: http://dx.doi.org/10.12989/was.2007.10.4.315

Proposed large-scale modelling of the transient features of a downburst outflow

W. E. Lin[†]

Department of Mechanical & Materials Engineering,
The University of Western Ontario, London, Ont., N6A 5B9, Canada

L. G. Orf[‡]

Department of Geography (Meteorology), Central Michigan University,
Mount Pleasant, MI, 48859, USA

E. Savory[†‡] and C. Novacco[‡‡]

Department of Mechanical & Materials Engineering,
The University of Western Ontario, London, Ont., N6A 5B9, Canada
(Received December 31, 2006, Accepted March 28, 2007)

Abstract. A preceding companion article introduced the slot jet approach for large-scale quasi-steady modelling of a downburst outflow. This article extends the approach to model the time-dependent features of the outflow. A two-dimensional slot jet with an actuated gate produces a gust with a dominant roll vortex. Two designs for the gate mechanism are investigated. Hot-wire anemometry velocity histories and profiles are presented. As well, a three-dimensional, subcloud numerical model is used to approximate the downdraft microphysics, and to compute stationary and translating outflows at high resolution. The evolution of the horizontal and vertical velocity components is examined. Comparison of the present experimental and numerical results with field observations is encouraging.

Keywords: downburst; microburst; outflow; localized high-intensity wind; wind tunnel; slot jet; wind loading; subcloud numerical model; cooling source.

1. Introduction

Meteorological field studies have identified downdrafts that persist to ground level as being potential severe wind hazards in the lowest portion of the troposphere. In particular, the term "downburst" refers to a convective downdraft that impacts on the ground and spreads outwards, often leaving a starburst damage imprint (Fujita 1985). Early studies, which were motivated by commercial aviation disasters,

† Graduate Student, Corresponding Author, Email: wlin25@uwo.ca
‡ Assistant Professor, Email: Leigh.Orf@cmich.edu
‡† Associate Professor, Email: esavory@eng.uwo.ca
‡‡ Former NSERC Undergraduate Researcher, now at Ontario Power Generation, Email: cnovacco@uwo.ca

categorized downbursts based on the spatial extent of the outflow. A length scale of 4 km (approximately the runway length at a large airport) was used to differentiate between "microbursts" and "macrobursts". As reviewed by Wakimoto (2001), several types of convectively-driven downdrafts have since been identified. Strong local downdrafts embedded within mesoscale convection systems, such as bow echoes and derechos, can leave a costly swath of damage. Furthermore, the rear-flank, forward-flank, and occlusion downdrafts are associated with supercell thunderstorms and appear to occur in concert with more localized phenomena (tornados and/or downbursts).

Downburst clusters are constituents of complex supercell flows. However, isolated downbursts of damaging intensity have also been observed to occur with little warning (Fujita 1985, Hjelmfelt 1988, McNulty 1991); although detailed records of extreme events are rare. The Andrews Air Force Base (AFB) downburst on 1 August 1983 yielded a 67 m/s peak gust at a propeller anemometer located 4.9 m above ground level (AGL) (Fujita 1985). This event appeared to be an isolated wet[1] downburst. More recently, Gast and Schroeder (2003) presented measurements of a rear-flank downdraft (RFD) on 4 June 2002 with 43 m/s gusts. However, given the current state of large-scale physical modelling in wind engineering, it is appropriate to focus on the low-level winds from an isolated downburst in the present work.

Fieldwork limitations are a significant obstacle to the study and forecasting of damaging events. Satellite imaging can track general storm motion but cannot discern internal structure. Lidar may be useful if clouds do not interfere with optical radiation (Doviak and Zrnić 1988). Doppler radar has been the instrument of choice, allowing detection of clear air downbursts associated with virga and study of the internal structure of thunderstorm cumulonimbi. Laboratory and numerical simulations that provide flow measurements at high temporal and spatial resolution supplement full-scale observations.

§ 2 reviews the previous approaches to simulation of the transient features of a downburst.

§ 3 discusses the primary considerations relevant to wind loading on structures. Subsequent sections pertain to the present numerical and experimental approaches whereby the outflow region is studied at high resolution and large physical scale.

2. Background

2.1. Previous experimental studies

Physical simulation of the transient features of a downburst, without translating environmental winds, has been performed by two methods:

(1) Impulsive release of a small fluid parcel into a large tank filled with fluid of lower density

Experimental conditions are described with the parameters defined in gravity current studies. The length scale (R_0) is the equivalent spherical radius of the cylindrical fluid release. The time scale, velocity scale, and flow Reynolds number are defined with Eqs. (1) to (3), respectively.

$$T_0 = \left(\frac{R_0 \rho}{g \Delta \rho}\right)^{0.5} \tag{1}$$

$$V_0 = \frac{R_0}{T_0} \tag{2}$$

$$\mathrm{Re}_\rho = \frac{R_0 V_0}{\upsilon} \tag{3}$$

[1]Observable precipitation at ground level (0.254 mm, Fujita 1985).

The large-scale features of the outflow were found to be independent of flow Reynolds number when the density differential and released parcel volume are sufficiently large ($Re_\rho > 3000$). In order to compare with results from the other simulation method, Table 1 provides downdraft and outflow information based on the container exit diameter (D_n). The velocity and length scales achieved with a density-differential-driven, impulsive release are extremely small.

The later experiments (Alahyari and Longmire 1995, Alahyari 1995, Yao and Lundgren 1996) refined the apparatus and technique of Lundgren, *et al.* (1992). Particle image velocimetry (PIV) results affirm that the extreme outflow velocities are attributable to a dominant, horizontal roll vortex. This roll vortex trails closely behind the outflow front. As a result, a stationary observer experiences a transient load, when the front/vortex passes by, due to the corresponding sharp horizontal gradient in horizontal velocity.

Table 1 Released fluid parcel simulations

Study	Buoyancy		Downdraft		Outflow		Comments
	$\Delta\rho/\rho$	Re_ρ	D_n [m]	Z_n/D_n	U_p[m/s] at (r/D_n)	data range [r/D_n]	
Lundgren, *et al.* (1992)	0.01 0.03 0.05 0.10	1377-6279	0.045	1.7 2.3	no data	no data	Agreement with a JAWS downburst for peak U/W and radial location of peak U.
Alahyari & Longmire (1995), Alahyari(1995)	0.03	3600	0.064	2.3 2.7	0.264* (0.74)	<1.23	Coarse PIV vector fields for the outflow region.
Yao & Lundgren (1996)	0.05	3077	0.045	2.3	0.248 (0.71)	0.282-2.82	Outflow velocities measured at $z/D_n = 0.028$ only.

*Peak value from azimuthal averages at fixed radial distances.

(2) Impulsively-started jet

Mason, *et al.* (2003, 2005) modified the round impinging jet apparatus that Letchford and Chay (2002) used for quasi-steady downburst simulations. A stationary nozzle approach was employed with a 16-blade gating device near the nozzle exit (similar to a camera iris), allowing a manually-actuated jet pulse. The gate actuation was non-linear with time since the duration required to open the initial 15% of the outlet area was the same as to open the final 85%. The quoted radial position of U_p in Table 2 may be an under-estimate, since the nozzle diameter is used as the normalizing value and the dominant vortex forms before the aperature is fully open. The radial position of peak outflow velocity in the quasi-steady simulations discussed in Lin and Savory (2006) was $r/D_n \approx 1$.

The opening time of the aperature in the experiments of Mason, *et al.* (2005) was similar to that achieved by Xu (2004) who used a valve for jet actuation. A sharp rise and decay was not apparent in the velocity history from the latter. A possible explanation is that the valve was located at greater than 60 D_n upstream of the nozzle exit.

The density differential that drives a downburst is modelled by the released fluid parcel approach. However, such experiments are extremely small-scale and produce low velocities. It is physically easier to generate intense flows using jets. However, the driving mechanism is the initial momentum supplied by blowing equipment rather than negative buoyancy.

2.2. Previous numerical modelling studies

Numerical simulations can provide insight into aspects of downbursts that are difficult to study

Table 2 Transient impinging jet simulations

Study	Nozzle parameters			Aperature opening time [s]	Radial position of U_p [r/D_n]
	D_n [m]	z_n/D_n	Re_n^*		
Mason, *et al.* (2003)	0.51	1.7	≈340000	not reported	0.75**
Xu (2004)	0.22	1	≈176000	≈0.2	≈1
Mason, *et al.* (2005)	0.51	1.7	≈306000	0.2	0.75**

*Based on D_n and steady W_n.
**May be under-estimated.

experimentally or in the field. Proctor (1988, 1989) used an axisymmetric numerical model (TASS) with a constant grid spacing of 40 m to simulate the thermodynamics and microphysics that lead to intense downburst outflows. Proctor (1988) found that the computed instantaneous vertical profile of radial outflow velocity agreed with results from a laboratory experiment of a steady impinging jet (Bakke 1957) and full-scale measurements from NIMROD (Fujita 1981).

Violent motion of the atmosphere is typically associated with high convective available potential energy (CAPE), which is essentially the temperature difference between fluid parcels and the environment integrated over height (Stull 1995). However, in very low CAPE environments in the Western Plains of the United States, dry downbursts can produce F1 winds (32.5 m/s < U < 49.5 m/s). An environment conducive to dry[2] downburst occurrence exhibits:

1. a high cloud base (> 5 km AGL) and a thick subcloud layer with an approximately dry-adiabatic lapse rate (Wakimoto 1985), and
2. dry air near the melting level and moist air near the surface (Proctor 1989).

The combination of a statically neutral environment and enhanced negative buoyancy associated with phase change of hydrometeors (i.e. melting in wet downbursts, and evaporation and sublimation in dry downbursts) can lead to downdraft speeds approaching 20 m/s. However, no clear relationship is apparent between peak horizontal outflow speed and peak downdraft speed. Proctor (1989) found this ratio to be very sensitive to environmental conditions (temperature and humidity profiles), downdraft radius, and precipitation type.

The dynamic equations for the full thermodynamics and microphysics are computationally expensive to solve. As a preliminary wind engineering study, Selvam and Holmes (1992) simplified the problem to a two-dimensional, steady, incompressible Navier-Stokes equation and applied the k-ε turbulence model closure. The non-dimensional vertical profile of outflow velocity ($z/z_{0.5}$ vs. U/U_m) predicted larger velocities near ground level than the corresponding peak profile from Proctor (1988).

Lundgren, *et al.* (1992) used a model based on inviscid vortex dynamics to investigate the development of the vortex ring. Although the outflow region was modelled at low spatial resolution, for a representative event, the following results were comparable to those from a full-scale downburst in neutrally stable conditions: (1) $U_m/W_{\min}$, (2) radial location of U_m, and (3) characteristic time. Surface friction produced counter-vorticity that retarded and elevated the dominant roll vortex, in agreement with Proctor (1988).

Orf, *et al.* (1996) and Orf and Anderson (1999, hereafter referred to as OA99) introduced a dry,

[2]No observable precipitation at ground level (<0.254 mm, Fujita 1985).

subcloud model referred to as the Wisconsin Model Engine (WME), which was designed to simulate downburst flow dynamics at high resolution. Microphysical cooling is modelled using a cooling function, whose parameters are prescribed to produce outflows that resemble field observations. Small flow structures can be discerned, and complexities such as colliding outflows and environmental wind shear were investigated. The present numerical work implements this conceptual approach with the Bryan Cloud Model (CM1, Bryan and Fritsch 2002) at high resolution, as described in § 5.

3. Key considerations for transient outflow simulations

The following issues arise for time-dependent simulation of outflows:

a) Vertical profiles of horizontal velocity from radar measurements are shown as resembling a wall jet profile (Fujita 1981, Hjelmfelt 1988). However, these downburst outflow profiles are extracted from Doppler radar scans between zenith and horizon. Strictly speaking, these earlier studies do not capture instantaneous profiles if the radar scanning time is significant relative to the downburst duration (2-15 min). It is of interest to examine true instantaneous profiles that coincide with the occurrence of peak horizontal outflow velocity. Furthermore, how do the profiles evolve with time?

b) From the perspective of a stationary object, a burst front passes as a sudden and short-lived event. Anemometer records of the outflow exhibit an abrupt rise in velocity, with the peak gust lasting briefly. Prior to $t = 700$ s in Fig. 1, the velocity history of the Andrews AFB downburst outflow shows little warning of the impending intense gust. The rise to the leading side peak gust and the corresponding average duration[3] each last for approximately 1 min.

Some nomenclature should be clarified before proceeding. In this article, "maximum" wind speed refers to the largest value over space at a specific time. "Peak" wind speed refers to the largest value over time at available spatial locations. If complete flow field data is available over time and space, such that the largest overall value for an event can be identified, this value is referred to as the "peak maximum".

Fig. 1 relates the velocity history features to various regions of the flow as the downburst translates past the anemometer. Inset 1 indicates that the extreme wind region on the leading side is responsible for the initial velocity peak. The subsequent lull in wind speed corresponds to the eye of the downburst shown in Inset 2. The back-side outflow in Inset 3 is detected as the second peak in the velocity history. The variation of wind direction during the event is also indicated, with the direction at $t = 0$ serving as the reference (0°). Wind direction is fairly constant until after the first velocity peak. As the eye of the downburst translates over the anemometer, the wind direction changes by approximately 180° as expected from the position of the anemometer relative to the flow in Insets 1 to 3.

The NIMROD and JAWS meteorological datasets had average durations of 3.1 and 2.9 min, respectively (Fujita 1985). More than 90% of the downbursts recorded had an average duration of < 5 min. Fig. 2 suggests that the duration of the peak outflow gust was slightly longer in Illinois downbursts than in Colorado ones, but the average duration distributions are comparable for these two studies in different climates.

[3]Defined as the duration for which $U > 0.5 \cdot U_p$.

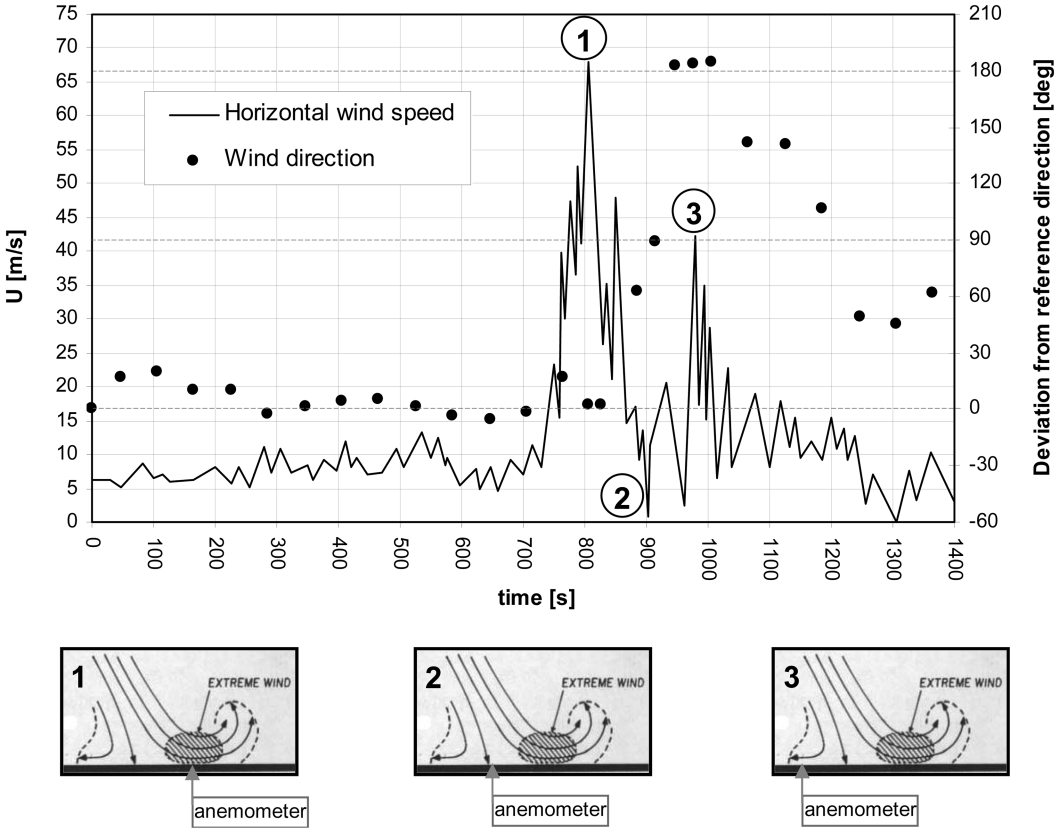

Fig. 1 Velocity history at 4.9 m AGL for a severe outflow (1 Aug 1983, Andrews AFB downburst data from Fujita 1985 and diagrams adapted from Wakimoto 2001)

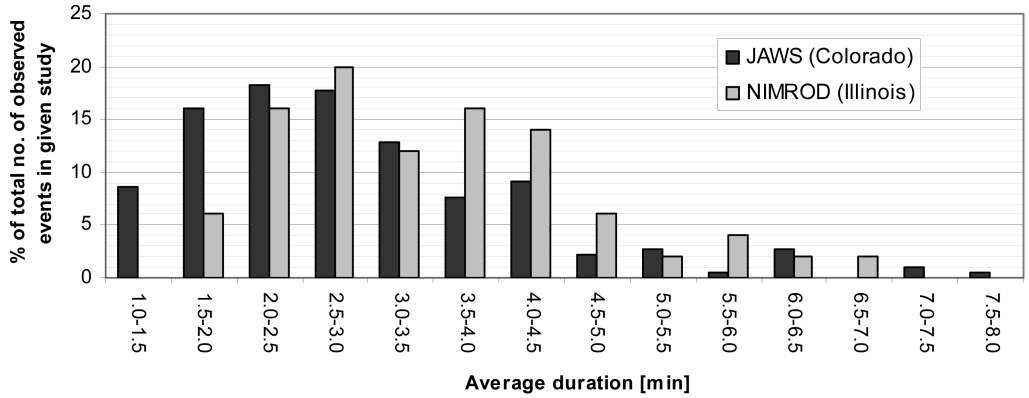

Fig. 2 Histogram of full-scale peak wind longevity (data from Fujita 1985)

c) Caracena (1982) proposed that a vortex ring develops about a non-translating (spatially stationary) downdraft. Subsequent observations corroborate that a vortex ring is indeed convected to the surface, at which point it spreads radially as part of the outflow. The opportune photographs in Fig. 3 show the vortical motion of entrained particles in the outflow as it advances leftward. With respect to a plan

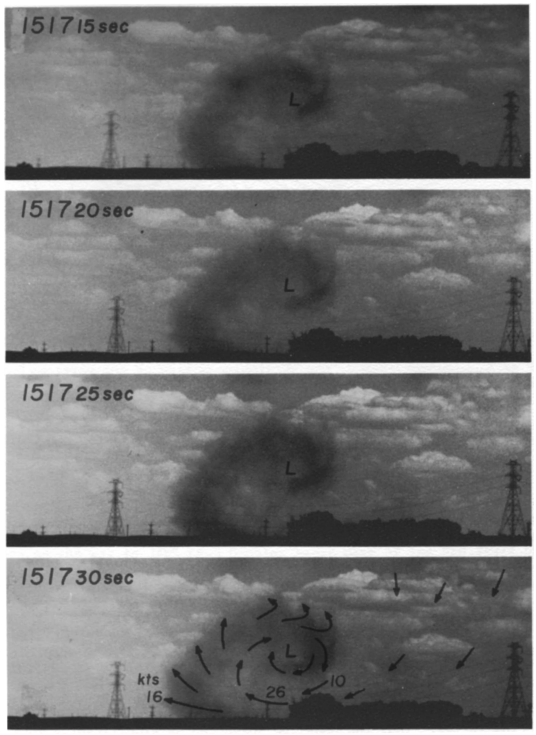

Fig. 3 A sequence of photographs for an outflow vortex from JAWS
(Reproduced from Fujita 1983 with photography by B. Waranauskas)

view, Fujita (1985) described a central high-pressure region associated with the downdraft stagnation point, which was encircled by a low-pressure ring. Time-dependent simulations indicate that a dominant, horizontal roll vortex is a primary feature of the outflow region (Proctor 1988, Lundgren, *et al* 1992, Mason, *et al.* 2005).

e) The downburst outflow is a statistically non-stationary process, and so it is problematic to quantify the gustiness with conventional definitions of turbulence quantities. Choi and Hidayat (2002) found that it is more appropriate to use fluctuations about a moving average to characterize the turbulent velocity component. An averaging time of 60 s was suitable for thunderstorm data from Singapore. Holmes and Hangan (2006) applied this approach to outflow velocity histories from a Texas RFD (Gast and Schroeder 2003).

Wavelets are particularly suitable for analysing signals with abrupt changes, such as the peak gusts in Fig. 1. For a Texas RFD and derecho, Chen and Letchford (2005) used wavelet shrinkage and a two-stage moving average method to infer the time-varying mean and standard deviation wind speeds, respectively. Proper orthogonal decomposition indicated that essentially all of the energy is located in the first mode for mean speeds, standard deviations, and normalized fluctuations.

The current state of meteorological knowledge indicates that intense convectively-driven downdrafts are distinct features of supercells (Wakimoto 2001). In the 2002 Thunderstorm Outflow Experiment near Lubbock, Texas (Gast and Schroeder 2003, 2004), seven mobile towers up to 15 m in height were deployed in a line arrangement, with the tower instrumentation primarily sampling at 2 Hz. The following extreme wind events were observed in June 2002: (1) a RFD of a non-tornadic

supercell and (2) a derecho.

Analyses of the RFD suggest that the outflow is well-correlated over a lateral extent of at least 789 m (Chen and Letchford 2006, Holmes and Hangan 2006). Although it appears possible to model an RFD outflow as being two-dimensional for wind engineering purposes, the present work focuses on simulation of isolated downbursts. Aside from observations suggesting that the RFD is a larger phenomenon than an isolated downburst, the former is more complex in origin and morphology than the latter (cf. Fig. 7.7 in Wakimoto 2001). The RFD is specific to a supercell and occurs in a high-shear environment, which is usually not accounted for in basic downburst modelling. Generalizing wall jet models from individual downbursts to more complex convective downdraft outflows is presently speculative.

f) Incidentally, in the meteorological literature, the general term "thunderstorm outflow" is occasionally used to refer to gust fronts (Goff 1976, Droegemeier and Wilhelmson 1987). These outflows are generally weaker and an order of magnitude larger in lateral extent than intense downburst outflows, and are described by the gravity current model (Charba 1974). Linden and Simpson (1985) briefly present their gravity current experiments in the context of downbursts, however, some fundamental differences appear in the results of gravity current and downburst experiments. In the former, there is frontogenesis, which is the "sharpening up of horizontal gradients to form a front" (Linden and Simpson 1986). The vorticity in a gravity current is related to the shielding of dense fluid from ambient fluid by a stable density interface. Since dense fluid from the rear is unable to move past the propagating front, it circulates up and to the rear of the horizontal flow, forming the characteristic head of the gravity current (cf. Fig. 1 from Droegemeier and Wilhelmson 1987).

On the other hand, the vortex formation in the downburst is initiated prior to the outflow stage. In physical experiments, Lundgren, *et al.* (1992) found vortex ring development due to baroclinic vorticity generation after the released parcel had fallen less than 1 D_n. The released parcel deforms and draws ambient fluid into the core of the downdraft column. Their axisymmetric, subcloud, numerical model also indicated that the vortex ring is initiated aloft about the downdraft column. Although the mixing effect of diffusion is neglected, the winding of the density discontinuity interface continues and intensifies in the outflow region.

Laser-induced fluorescence visualization by Alahyari (1995) also suggests significant interaction between ambient and released parcel fluid at the location of peak outflow velocity. In contrast, mixing in the gravity current occurs in the turbulent wake, after the dense fluid has circulated from the rear past the nose and head regions. The gravity current model may be applicable during the later, dissipating stage of the downburst outflow, but not at peak intensity.

4. Experimental simulation

Field observations (Fujita 1985, Hjelmfelt 1988) and buoyancy-driven numerical simulations (Proctor 1988, Orf, *et al*. 1996) indicate that a downburst outflow has a highly time-dependent nature due to a dominant horizontal vortex. Dynamically similar experiments appear to be important for structural design since there may be speed-up associated with the dominant roll vortex, relative to an equivalent quasi-steady outflow (Chay and Letchford 2002, Mason, *et al*. 2005). Simulation of the transient features outlined in § 3 is crucial for structures that are particularly sensitive to impulsive loading. The quasi-steady slot jet approach is readily extended to model the transient features of the downburst outflow.

4.1. Test facility

The test facility introduces a slot jet into the working section of an atmospheric boundary layer wind tunnel as described in detail in the preceding companion article (Lin and Savory 2006). A rectangular slot nozzle is installed across the working section span and is flush with the ground plane, allowing the slot jet to develop into a 2-D wall jet. The slot aspect ratio (Y/b) is 24. The co-ordinate system origin in the prototype facility test section is fixed at the spanwise centreline of the nozzle exit, at the ground plane of the test section as shown in Fig. 4.

Fan speed is held constant, so that the transient slot jet is produced solely by the gate actuation. Since the purpose of the prototype facility is to investigate the feasibility of a slot jet model of the downburst outflow, further complexities such as a co-flow above the slot top are not implemented in the prototype. A co-flow configuration can potentially be used to model a downburst with "surface environmental wind" (cf. Hjelmfelt 1988, p. 906) or a downburst embedded in a translating storm (Holmes and Oliver 2000). The full-size facility will have the capability to augment the transient wall jet with a co-flow.

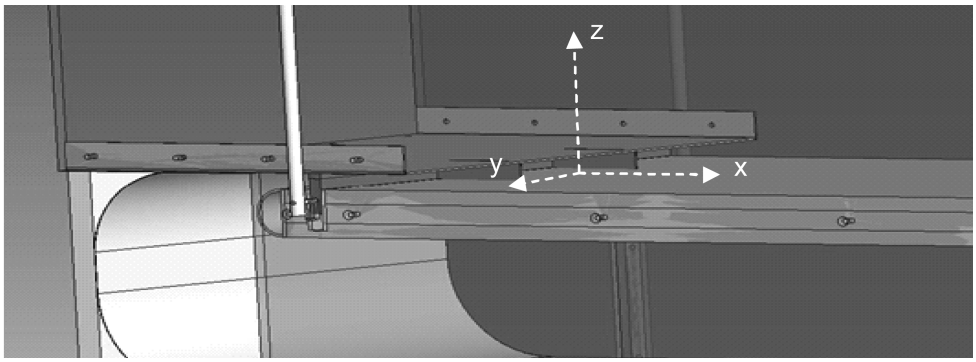

Fig. 4 Coordinate system in the slot jet facility

To minimize potential disturbances from external air and to approximate the conditions in the full-size facility, a coarse screen is installed at the prototype test section inlet indicated in Fig. 5. Aside from the screen, external air is free to be entrained into the working section. Two gate designs were implemented in the 1:7 scale prototype facility.

4.1.1. Translating gate

The assembly in Fig. 5 allows the flow to be actuated with a linear motion gate. Each realization of the transient flow begins with the gate shut (at its highest vertical position). The fan operates under steady conditions and pressurizes the duct and slot. A static pressure port on the side wall behind the gate allowed the pressurization to be monitored to ensure consistency between slot jet actuations. When the gate is quickly translated downwards until its top surface is flush with the $z = 0$ plane, the static pressure behind the gate converts to the dynamic pressure of the slot exit velocity (U_j). After reaching the fully-open-slot position, the gate immediately returns to the fully-shut-slot position. To improve the seal of the fully shut slot and reduce the impact on the slot top, a thin layer of rubber foam is attached to the top surface of the gate. Opening and closing durations of 0.10 and 0.19 s, respectively, are achieved. The objective is to reproduce a velocity history rise and decay that matches field observations.

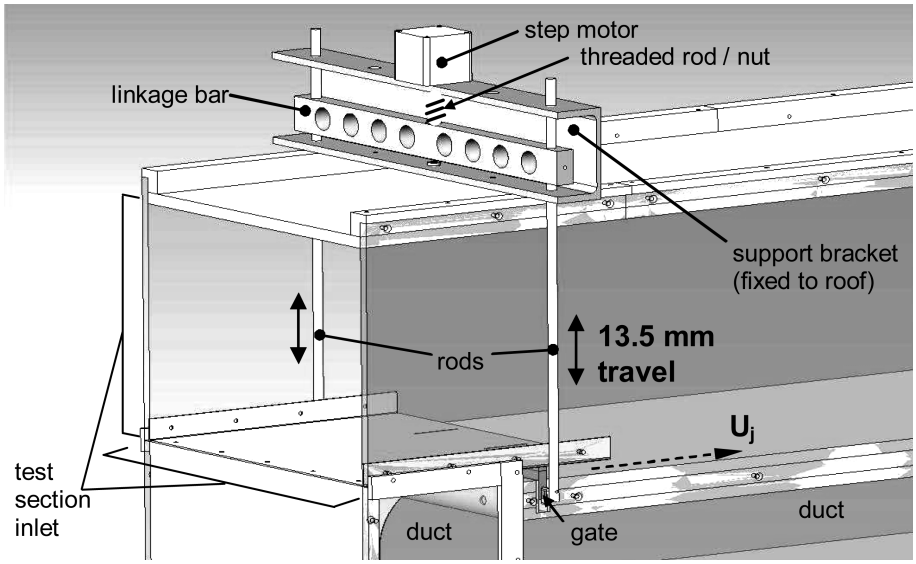

Fig. 5 Linear motion gate assembly

The stainless steel gate is driven by a step motor mounted above the tunnel. The gate, rods, and linkage bar in Fig. 5 are a rigid assembly. The step motor is fixed to the C-section support bracket. A precision, multi-threaded rod is coupled concentrically to the step motor shaft and the matching nut is fixed to the linkage bar. Thus, the rotary motion of the step motor shaft is converted into smooth linear gate motion (25.4 mm/rev or 200 steps/rev). A digital pulse train input allows repeatable gate positioning. In the powered standstill condition, the large holding torque of the step motor allows the gate to be held firmly shut.

As seen in Fig. 4, the gate is pinned to the rods through slots in the tunnel side walls. These slots do not affect the flow when the gate is open because the gate itself blocks off the entire slot. When the gate is fully closed, the slots are partially open but the close fit between the gate and adjacent components allows negligible leakage from the working section. The gate is restrained such that its only degree of freedom is vertical translation across the 13.5 mm slot height (b).

4.1.2. Rotating gate

The alternative gate design introduces a rod at the centre of the 13.5 mm slot height. Two 1.6-mm-thick steel flaps, welded onto the rod, form the gate. The gate is free to rotate in brass bushings that are press-fit into the tunnel sides. The starting position and initial direction of rotation for all of the experiments is shown in Fig. 6(a). Fig. 6(b) shows the sign convention for $\Delta\theta$ and illustrates the sequence of gate positions during an actuation. There is no pause when the slot is in the fully open condition.

The following gate sequences are studied: (1) a half-revolution in one direction ($\Delta\theta = +180^{o}$) and (2) two quarter-revolutions with an intermediate change in direction ($\Delta\theta = +90^{o} - 90^{o}$). The step motor described in § 4.1.1 is relocated to drive the rotating gate. Total actuation times of 0.10 and 0.20 s are investigated, where the opening and closing phases are of approximately equal duration.

At Position 2 shown in Fig. 6(b), blockage of 26% of ($Y \cdot b$) is incurred due to the rod at the slot mid-height. However, results in § 6 show that a significant wake is not evident in the downstream velocity profiles and that the velocity histories are more repeatable than those obtained with the

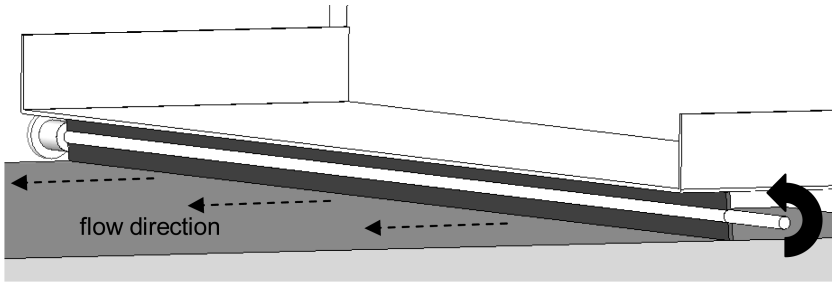

Fig. 6(a) Perspective view of the starting position of the rotational motion gate

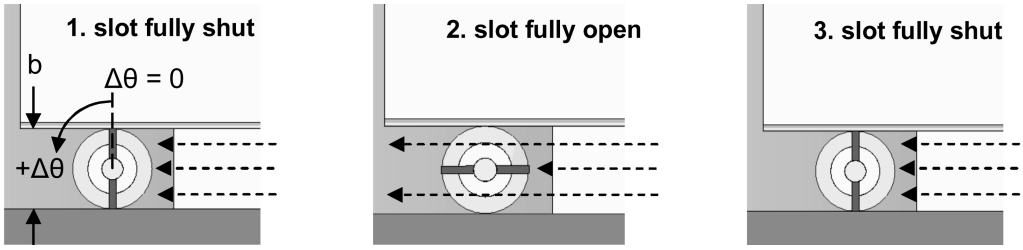

Fig. 6(b) Side view depicting the extreme slot conditions during continuous rotational gate actuation

translating gate. However, sealing the slot in the fully closed position is challenging, and the observed leakage is ~25% of the peak horizontal velocity.

4.2. Velocity measurements

The cross-wire (x-wire) anemometry set-up described in Lin and Savory (2006) enables a velocity sampling rate of 10 kHz. The x-wire and gate systems are synchronized so that data acquisition and gate actuation start simultaneously. Ten realizations ($n = 10$) are performed at each x-wire location for the translating gate tests. For the rotating gate, $n = 5$ since improved repeatability was observed. Velocity histories at each x-wire location are graphed together and inspected for anomalous realizations that are due to occasional inconsistent gate actuation (likely resulting from slight variations of friction in the mechanical system). These realizations are excluded from subsequent analysis. The accepted histories are ensemble-averaged to give a composite velocity history ($<U>$) at $N = 50$ probe locations. Vertical profiles are constructed as shown in Fig. 7 and the temporal development of the composite profile is determined.

Hot-wire anemometry is an intrusive technique that can affect the flow if the inserted apparatus is too large. Verhoff (1970) extensively investigated the effect of a 6.35 mm diameter rod on a transient 2-D slot jet. Photographs at 800 fps, as well as hot-wire outputs, did not show any noticeable influence of the rod on dominant roll vortices. The probe holder diameter in the present apparatus is 6 mm and the L-shaped holder places the probe upstream of the vertical support tube.

X-wire probes give accurate results only when the flow approach angle remains within the cone of acceptance of ±45° with respect to the probe axis (Jørgensen 2005). The instantaneous approach angle generally remained < 20° in the region of interest (maximum value of 27°). Measurements in the outer region of the wall jet were less reliable because of the high local turbulence intensity there. The flow reversal of the dominant vortex is not discerned due to signal rectification. Since the

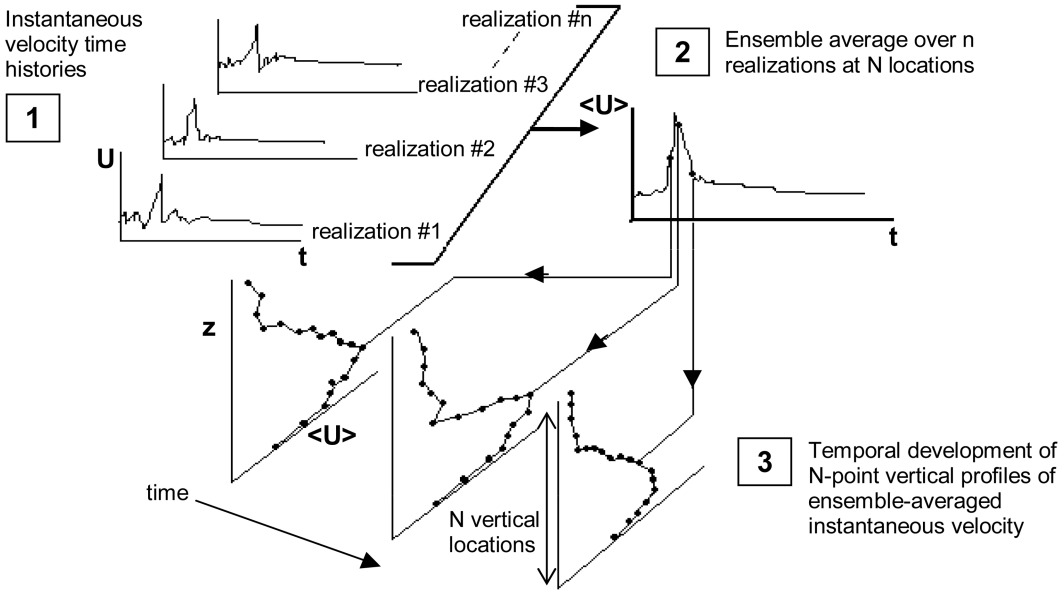

Fig. 7 Data flow for transient jet results

region of present interest is near the maximum of the vertical profile of mean streamwise velocity, signal rectification does not limit the applicability of the present measurements.

5. Numerical simulation

A dry version of the Bryan Cloud Model (CM1) is employed in the present numerical study. It is a non-hydrostatic, three-dimensional model designed for simulation of cloud and subcloud phenomena (Bryan and Fritsch 2002). Prognostic equations for wind velocity, non-dimensional pressure, and potential temperature are solved. The model is integrated with third-order Runge-Kutta time differencing and sixth-order spatial derivatives for advection terms. Subgrid turbulence closure is handled by a k-ε scheme that solves prognostic equations for turbulent kinetic energy and turbulent kinetic energy dissipation. A time-splitting technique (Klemp and Wilhelmson 1978) is implemented, which integrates acoustic waves with a shorter time step than the physical model time step.

The approach regarding forcing the downburst is identical to that of OA99 where a spatial- and time-dependent cooling function serves as a forcing term in the prognostic equation for potential temperature. In the same spirit as the simulations presented in OA99 and Orf, *et al.* (1996), the focus is on producing a realistic downburst by parameterizing the thermodynamic cooling found in a downburst-producing thunderstorm, without modelling the microphysical processes found in such a storm. Essentially, the development of a cooled volume of air in a dry adiabatic environment is studied with the present approach.

The most straightforward way to simulate a surface flow that is consistent with a significant wind loading event is to increase the OA99 temperature perturbation magnitude. The present numerical simulations use a cooling forcing shape identical to that described in OA99, but the intensity of the cooling has been increased by a factor of four. This adjustment provides sufficient negative buoyancy to force an intense downdraft with resulting horizontal winds that reach damaging

intensity. A more realistic forcing would include microphysics and model an entire downburst-producing thunderstorm, but this gain in realism would come at the expense of grid resolution and integration time, in order to accommodate the much larger model domain that is required.

The model is run on a C grid (Arakawa and Lamb 1977). The 40 grid points closest to the surface are spaced 5 m apart in the vertical direction; above this, the grid is stretched to 25 m spacing at the top of the model domain (3.8 km AGL). The grid point closest to the surface is at 2.5 m AGL. Vertical resolution is enhanced near the ground in order to sufficiently resolve the vertical flow structure in this region of interest. The horizontal grid spacing is a constant 10 m throughout the simulation domain. The model uses open lateral boundary conditions and a semi-slip bottom boundary condition with a constant drag coefficient of 1.67 x 10^{-3} (reference wind speed at closest grid point to the surface). This C_{DN} value produces an outflow head structure that is consistent with observations (e.g. Fig. 3). For reference, this C_{DN} value corresponds to $z_0 = 0.0001$ m (calm, open sea terrain) for a steady logarithmic wind profile (Stull 1988, pp. 262-267).

6. Discussion of results

Following the slot jet experimental results in § 6.1, the velocity field histories from the CM1 numerical simulations are presented in § 6.2. Both horizontal and vertical velocities are examined in the numerical work. The present numerical and experimental results are then compared with available field data. As mentioned in § 3, the velocity profile shapes and how the intense flow regions evolve in time are particularly relevant to wind loading of structures.

6.1. Slot jet results

6.1.1. Flow visualization

The dominant roll vortex in the transient 2-D slot jet flow is visualized by filling the slot and anterior duct with a fog fluid (low-molecular-weight glycol and de-ionized water vapour). The gate actuation generates a dominant vortex near the leading edge of the streamwise propagating front. In Fig. 8, a simple tower model is located at $x/b = 20$ and the roll vortex axis is at $z/b \approx 4.5$.

Verhoff (1970) investigated pulsing a 2-D slot jet at $\geq$ 1 Hz. The continuous stream of turbulent vortices reached a developed state at $\approx 100\ x/b$, independent of the pulse rate, pulse shape and uniform co-flow velocity. An increase in co-flow velocity decreased $\partial z_{axis}/\partial_X$, likely because of (1) an increased restraining influence of the co-flow on the slot jet and (2) a decrease in time for vertical growth since the vortex is advected downstream more rapidly.

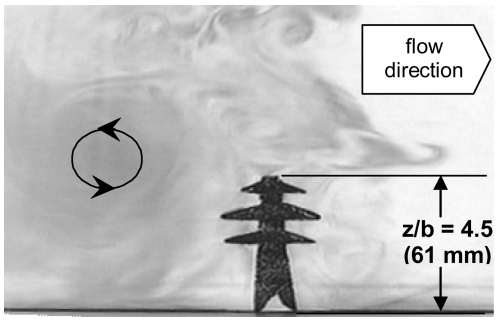

Fig. 8 Transient simulation vortex from prototype slot jet facility

6.1.2. Lateral correlation of vertical profiles

Verhoff (1970) observed two-dimensionality of a pulsed slot jet at the slot exit ($x/b = 0$), based on smoke visualization and total head probe measurements that indicated total pressure varied by less than ±1% of the maximum value away from the flow boundaries. The transient wall jet in the present prototype facility retains two-dimensionality as shown in Fig. 9. $<U>$ is normalized by the corresponding steady velocity at $x = 0 = y$ and $z/b = 0.5$ (i.e. the fan is in steady operation, as in the transient tests, but the gate is fixed in the fully open position). For all of the present results, $U_{j,\ steady} = 45$ m/s. Profiles are shown for $t = 0.07$, 0.10, and 0.12 s after the gate begins opening. The largest variation between profiles is at $t = 0.12$ s and $z/b = 0.56$, where the $y/Y = +0.22$ profile decays to 83% of the centreline profile. Furthermore, transient round impinging jet experiments suggest that the dominant vortex ring is correlated over 0.25 D_n, which is estimated to be 400 m in full-scale (Mason, *et al*. 2005).

6.1.3. <U> profile evolution

The temporal development of the composite profiles at $x/b = 30$ is also shown by Fig. 9. It is evident that the maximum in the composite profile approaches the ground plane near the occurrence of peak $<U>$. These measurements are consistent with previous simulations that suggest the rotation of the dominant vortex results in dynamic speed-up of the outflow (Proctor 1988, Lundgren, *et al.* 1992). Mason, *et al.* (2003) found that the ensemble-averaged peak velocity, over 5 realizations of the transient impinging jet, exceeded the corresponding peak mean velocity in the steady impinging jet (Chay and Letchford 2002) by greater than a factor of two.

6.1.4. Turbulence intensity

For time-dependent wind events, the velocity history should be separated into time-varying mean

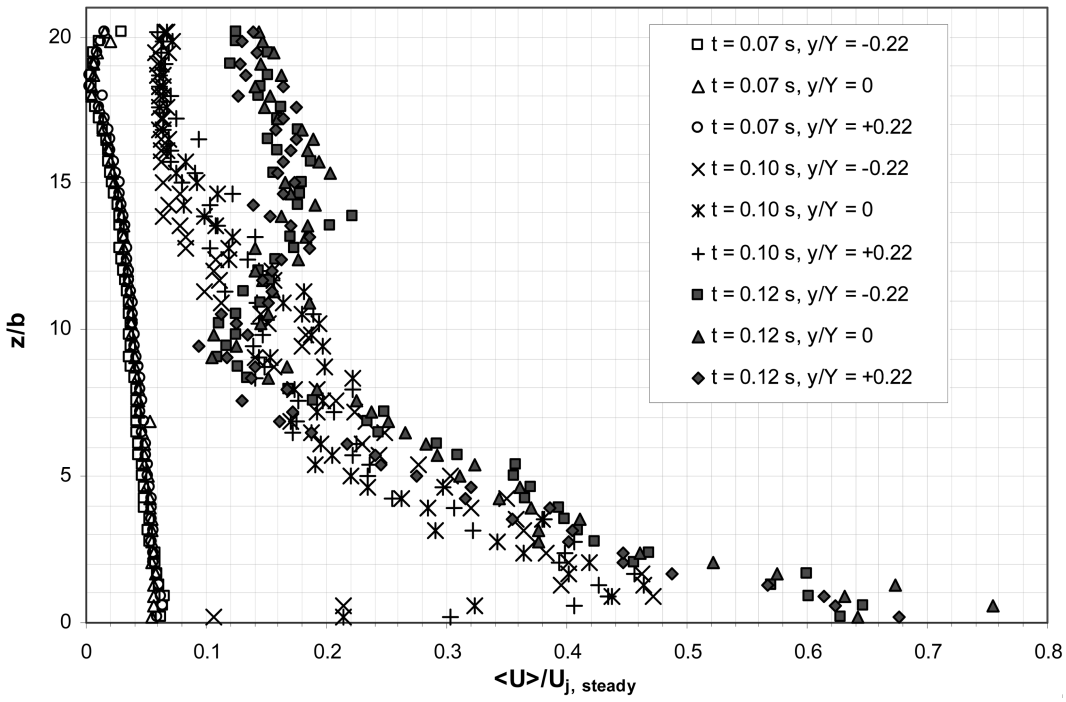

Fig. 9 Composite profiles at $x/b = 30$ in the slot jet prototype facility with translating gate

and residual fluctuation components (Choi and Hidayat 2002). Fig. 10 presents a weighted 3-point moving average for the anemometer field record shown in Fig. 1. The moving average value at a given time, $U_{MA}(t_s)$, is calculated as follows:

$$U_{MA}(t_s) = \frac{w_1 \cdot U(t_{s-1}) + w_2 \cdot U(t_s) + w_3 \cdot U(t_{s+1})}{w_1 + w_2 + w_3} \tag{4}$$

where s is the ordered sample number, $w_1 = w_3 = 0.2$ and $w_2 = 0.6$. Without weighting, the U_{MA} peak tends to precede the U peak.

The discernable time resolution of the Andrews AFB anemometer data is not high, so an effective turbulence intensity ($\hat{I}_u$) is estimated as being the ratio of the instantaneous deviation (U-U_{MA}) to U_{MA} at the same instant. At the time of peak velocity in Fig. 10, $\hat{I}_u \approx 25\%$ at 4.9 m AGL. A similar analysis is applied to velocity histories from the present slot jet experiments. The slot jet data is sampled at 10 kHz, so a 70-point moving average is employed to smooth the velocity history, whilst retaining the velocity peak associated with the roll vortex. At the height and time of peak velocity at $x/b = 30$ and $y = 0$, the actuated slot jet yields $\hat{I}_u$ between 20 and 30%. This $\hat{I}_u$ range is based on analysis of 9 realizations of the translating gate outflow.

With high time resolution data from the 2002 Thunderstorm Outflow Experiment, other investigators used more involved approaches to calculate effective turbulence intensity. Chen and Letchford (2005) employed a two-stage weighted moving average method, with a window width of 32 s, to estimate the time-varying standard deviation. At 4 and 6 m AGL, the effective turbulence intensity near the peak time-varying mean wind speed was approximately 8 and 15% for the RFD and derecho events, respectively. For the RFD event, Holmes and Hangan (2006) used the ratio of the time-varying root-mean-square (r-m-s) of residual fluctuations to the time-varying mean velocity. The time-varying r-m-s and mean were both calculated based on a 40 s window width. At 10 m AGL,

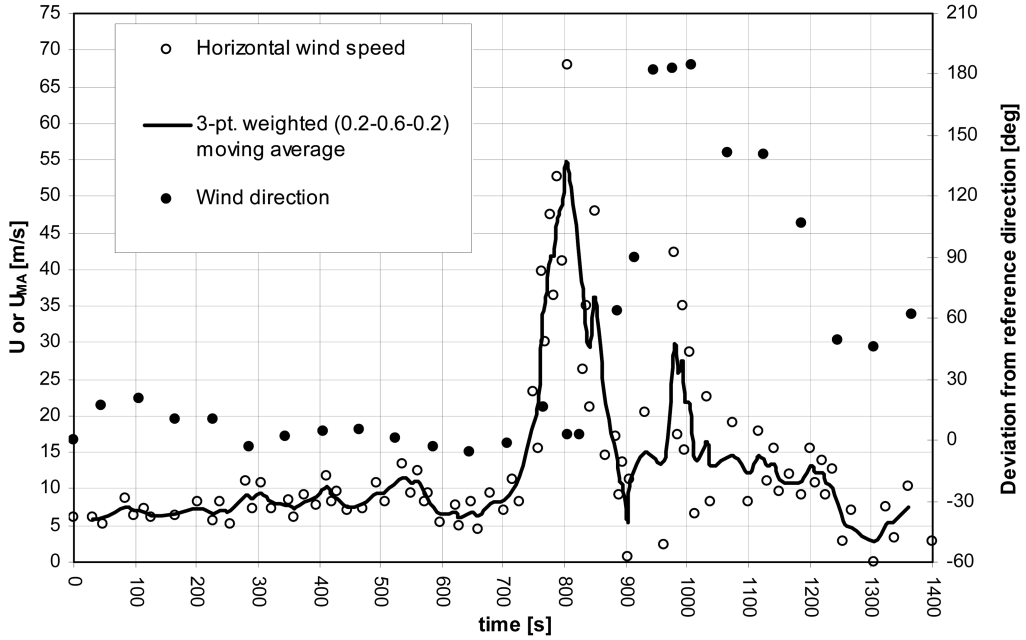

Fig. 10 Moving average for the Andrews AFB downburst outflow wind speed history

the effective turbulence intensity was ≈ 10% at the peak time-varying mean velocity and reached approximately 25% during the rise to this peak.

6.1.5. Comparison of flow with translating and rotating gate designs

Fig. 11 compares peak <*U*> profiles from the translating and the rotating gate designs. Fan operating conditions are consistent between all of these experiments. A total actuation time (t^*) of 0.29 s was the fastest translating gate actuation achieved. Two rotating gate sequences (cf. § 4.1.2) with two different t^* values (0.10 and 0.20 s) are investigated.

Compared with the translating gate peak profile, the maximum in the rotating gate peak profiles occurs at larger *z*. There is a distinct maximum in the rotating gate profiles, and as may be expected from the direction of rotation indicated in Fig. 6, the flow near the wall is slowed. The $\Delta\theta = +180^o$ gate sequence slows down the near-wall flow more than the $\Delta\theta = +90^o\text{-}90^o$ sequence. In the former, the lower half of the gate is always moving against the flow. In the latter, the lower half of the gate moves against the flow for the first half of its motion and with the flow for the second half. Changing the rotating gate t^* by a factor of two does not significantly affect the resulting <*U*> profiles.

6.2. CM1 results

Three numerical simulation cases are presented in this study. All cases use a cooling function with a horizontal half-width of 1200 m, but it is more physically meaningful to normalize the computed results by a length scale that is representative of the downdraft diameter which develops during the transient simulation. At the height of peak *W* magnitude and after the dominant roll vortex passes, *D* ranges between 1400 and 1650 m in all cases, based on the horizontal extent where $W < -3$ m/s. Thus, $D = 1500$ m is used in normalizing the following CM1 results.

Cases 1 and 2 simulate a non-translating, axisymmetric, isolated downburst. The cooling source is

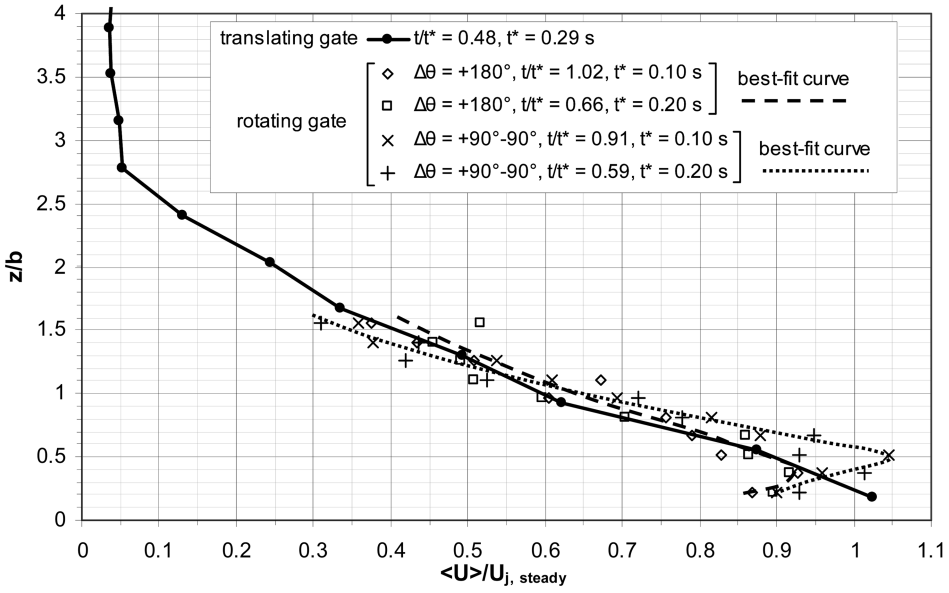

Fig. 11 Comparison of centerline peak composite profiles at $x/b = 10$ for the two gate designs

fixed at a single location with a cooling forcing of shorter duration in Case 2 than in Case 1. The peak maximum velocity ($U_{p,\max}$) occurs at 320 and 326 s into the simulation for Cases 1 and 2, respectively. $U_{p,\max}$ in Case 2 (37 m/s at $z/D = 0.005$ and $r/D = 1.11$) is significantly reduced from that in Case 1 (47 m/s at $z/D = 0.005$ and $r/D = 1.17$) as expected.

The potential flow solution for a stagnation point flow assumes that U increases linearly from the stagnation point out to r/D where peak U occurs (Holmes and Oliver 2000 after Schlichting 1979, p. 101). Comparing Figs. 12(a) and 13(a), the potential flow solution appears to be less valid at small z/D in Case 1 (stronger forcing) than Case 2. In Fig. 12(a), there is a local velocity increase ($U/U_{p,\max} = 0.659$

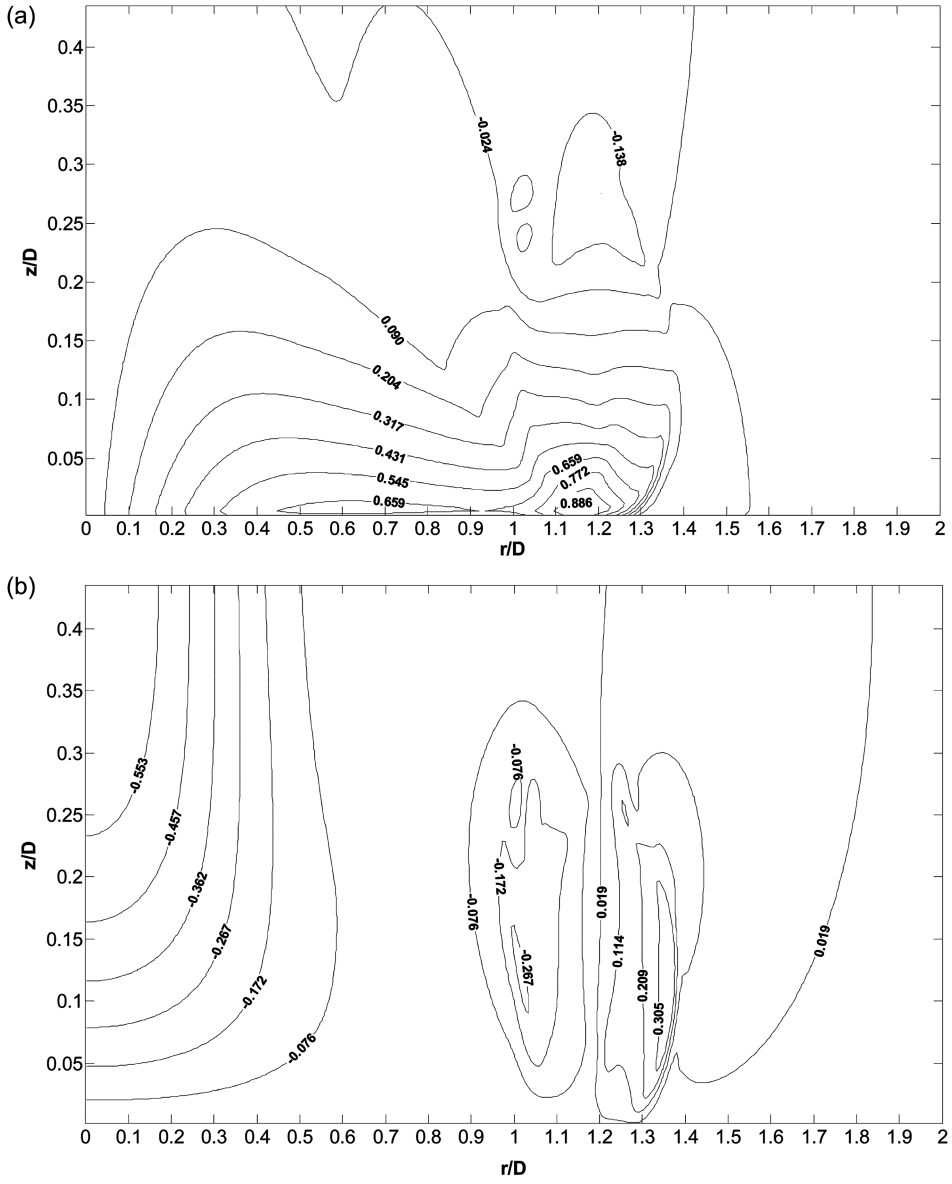

Fig. 12 Contours of (a) $U/U_{p,\max}$ and (b) $W/U_{p,\max}$ when $U_{p,\max}$ occurs in CM1-Case 1

contour) that occurs between the stagnation point and $U_{p,\max}$. Instead of an increase, there is a local velocity plateau in Fig. 13(a) between the stagnation point and $U_{p,\max}$. Figs. 12(a) and 13(a) show agreement with field observations of the horizontal velocity variation in the radial direction (Hjelmfelt 1988, Fig. 12). The effect of cooling forcing duration on the outflow velocity history is examined in § 6.4.

Figs. 12 and 13 give an indication that the occurrence of $U_{p,\max}$ coincides with essentially zero vertical velocity. In fact, $W/U_{p,\max}$ = -0.002 and 0.0004 at the location of $U_{p,\max}$ in Cases 1 and 2, respectively. The peak positive W, associated with the leading edge of the dominant vortex, is $W/U_{p,\max}$ = 0.4 in both Cases 1 and 2. These values occur at z/D = 0.125 and 0.167, respectively. The

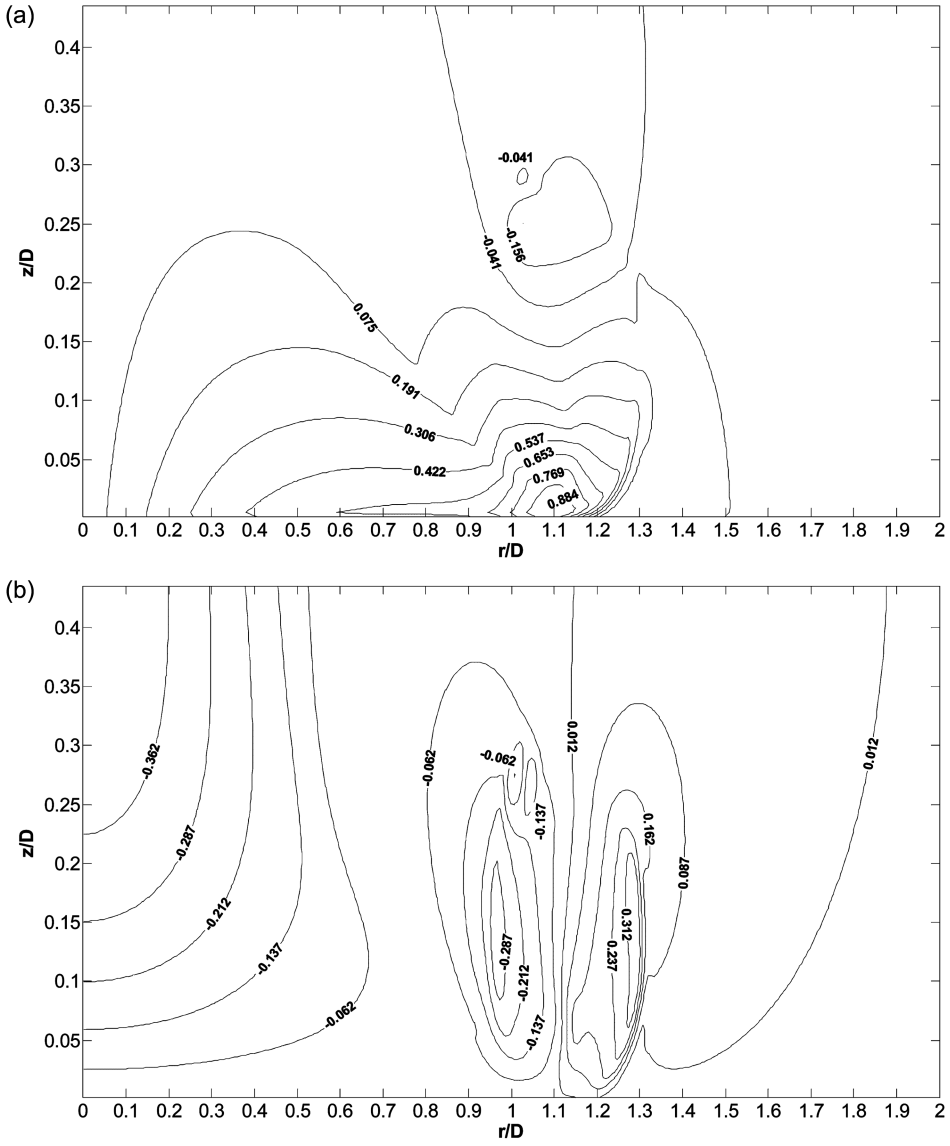

Fig. 13 Contours of (a) $U/U_{p,\max}$ and (b) $W/U_{p,\max}$ when $U_{p,\max}$ occurs in CM1-Case 2

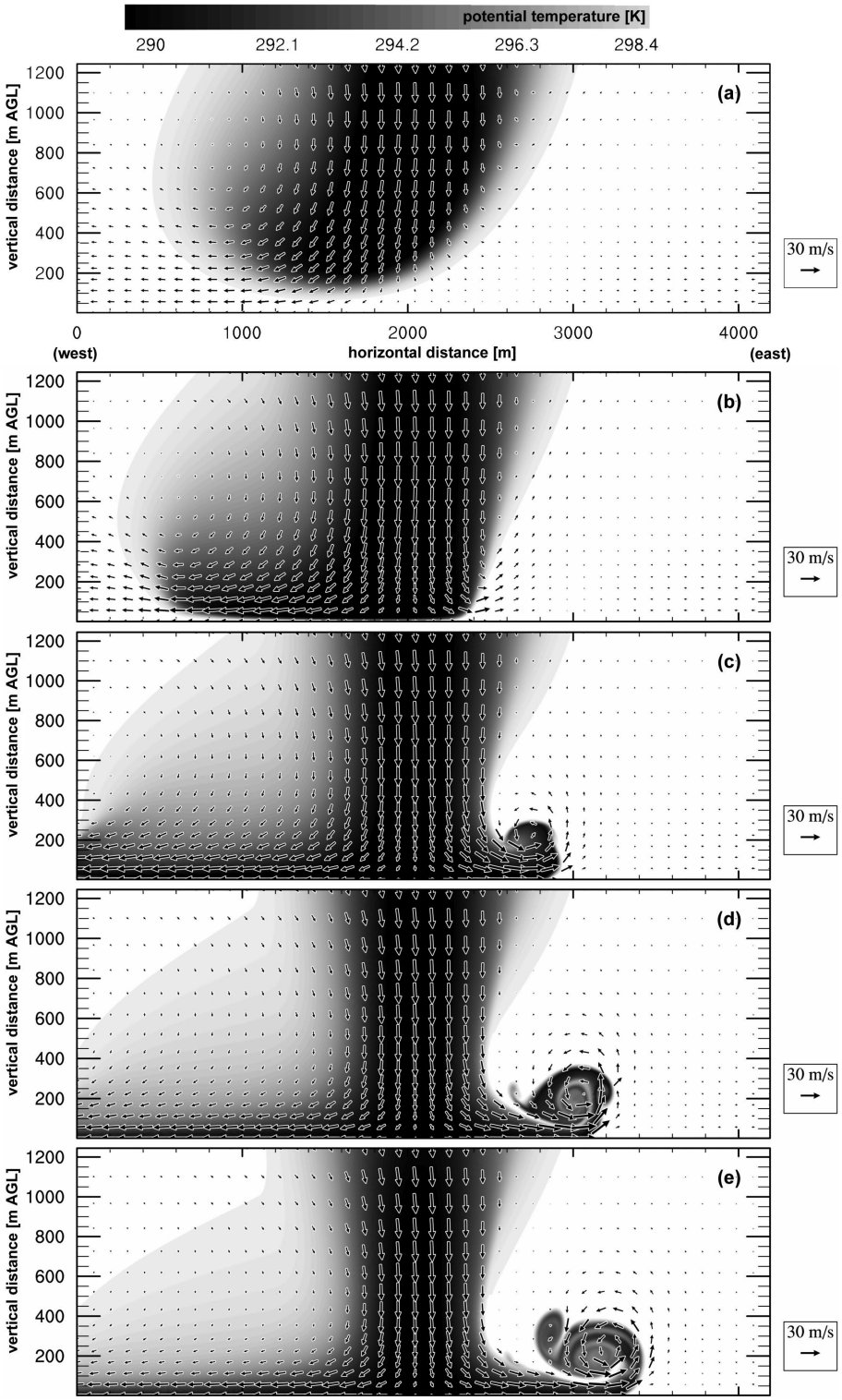

Fig. 14 Continued on following page

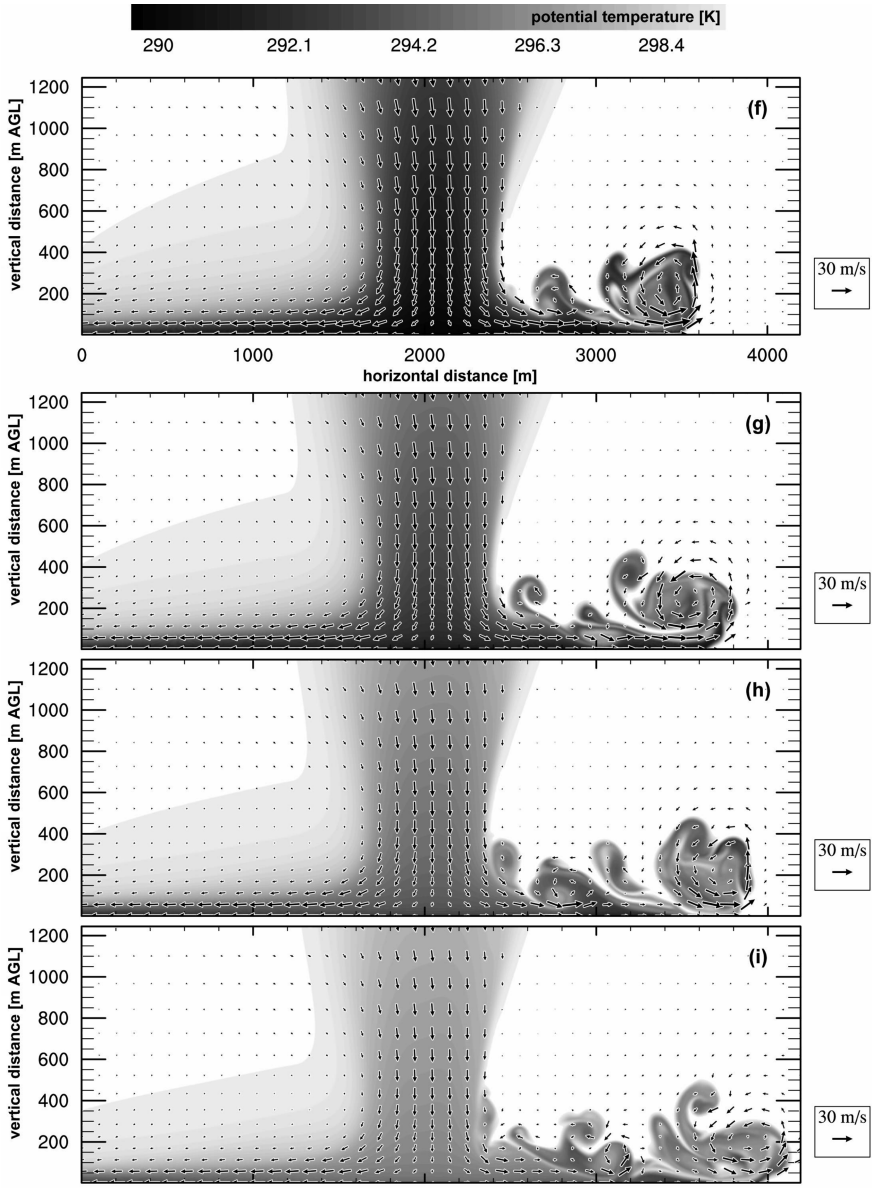

Fig. 14 Evolution of the velocity vectors (for clarity, vectors are shown at only every tenth gridpoint in both spatial directions) and potential temperature contours for CM1-Case 3 at the following times after the start of the simulation: (a) 210 s, (b) 240 s, (c) 270 s, (d) 300 s, (e) 330 s, (f) 360 s, (g) 390 s, (h) 420 s, and (i) 450 s

peak negative W, associated with the trailing edge of the dominant vortex, is $W/U_{p,\max} = -0.3$ in both Cases 1 and 2. These values occur at $z/D = 0.125$ and 0.135, respectively. In the lowest 50 m AGL, the extreme vertical velocities occur at radial locations between the peak maximum U and extreme W locations. These are $W/U_{p,\max} = 0.25$ and -0.11 for Case 1, and $W/U_{p,\max} = 0.23$ and -0.13 for Case 2.

Case 3 simulates a moving, isolated downburst by horizontally translating the cooling source, as in OA99. A Lagrangian perspective is taken, in the sense that the model domain follows the cooling

source as it moves eastward relative to the ground (cardinal directions indicated below Fig. 14a). The peak maximum horizontal gust (69 m/s) and constant translational speed of the cooling source (U_t = 8 m/s) are in close agreement with the observed peak speed and the baseline wind speed prior to the peak gust in the Andrews AFB event (cf. Fig. 1), respectively.

The cooled air in the simulation can be treated as air parcels that are distinct from the ambient environment. In the dry adiabatic environment, vertical motions of a cold air parcel do not affect its potential temperature. By regarding potential temperature as a passive tracer that is advected with the flow field, potential temperature contours give a fair indication of the corresponding velocity field, as shown by Fig. 14.

The first 500 s of the computed wind field is used to determine wind speed histories as experienced by two 653-m-high[4] stationary structures that encounter the simulated downburst outflow. The time resolution is 1 s. In Fig. 14, the geometric centre of the cooling source is fixed to the centre of the Lagrangian model domain (x' = 0) that translates eastward at a rate of 8 m/s. The initial location of Structure A is chosen to be the eastern edge of the model domain as depicted in Fig. 15 (x'/D = +1.397 at nt_A = 1). The model domain is spatially resolved into 420 horizontal grid points, and linear interpolation for velocity is done when the structure location lies between simulation grid points (i.e. when nt modulo 5 ≠ 1). For instance, at the last time step (nt_A = 500), Structure A lies between two grid points on the western side of the model domain.

Structure A encounters a peak U of 38 m/s at z/D = 0.005 and t_p = 240 s. Fig. 16(a) shows that, at z/D < 0.05, this positive peak U is followed shortly in time by a zero value and a negative peak U. As depicted in the Fig. 1 insets, these features of the U history correspond to the leading side outflow, the downdraft stagnation region, and the trailing side outflow, respectively. The peak westward U is 24 m/s at z/D = 0.005 and 123 s after Structure A encounters the peak eastward U.

Vertical velocities near the peak U/U_p contours are small compared to the corresponding horizontal velocities. W magnitude in Fig. 16b is less than 20% of U_p where and when U/U_p > 0.851 in Fig. 16(a). As the downdraft core passes over the structure, for z/D < 0.067 (< 100 m AGL), W is approximately inversely proportional to z.

In order for Structure B to encounter the peak maximum U gust in the Case 3 flow field at $t_{p,\max}$ = 405 s, its initial location is chosen beyond the eastern edge of the model domain (3.097 D

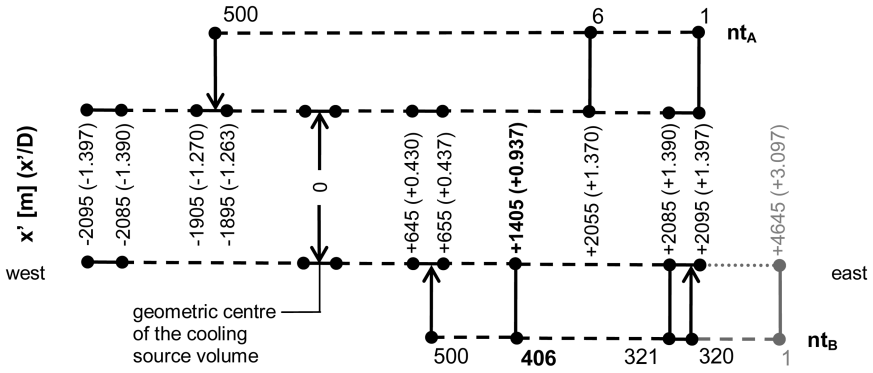

Fig. 15 Movement of Structures A and B through the computed flow field for CM1-Case 3

[4]The 653 m height corresponds to a computational grid point. Since the grid is graded above z 200 m, the upper boundary of the presented data does not coincide with a "round" number

eastward of the geometric centre of the cooling source volume). As depicted in Fig. 15, Structure B does not enter the simulated domain until $nt_B = 320$, when it lies between the 1st and 2nd gridpoints at the eastern edge. Structure B experiences the peak maximum gust (69 m/s) in the Case 3 flow field at $z/D = 0.005$, $x'/D = 0.937$, and $t_{p,\max} = 405$ s ($nt_B = 406$).

Fig. 17 reveals some interesting aspects of the trailing wake behind the dominant roll vortex (cf. Figs. 14f to i). Two distinct, trailing regions of rotational flow are identifiable. In addition to decreased U and W magnitudes, there are noticeable decreases in spatial extent and height AGL,

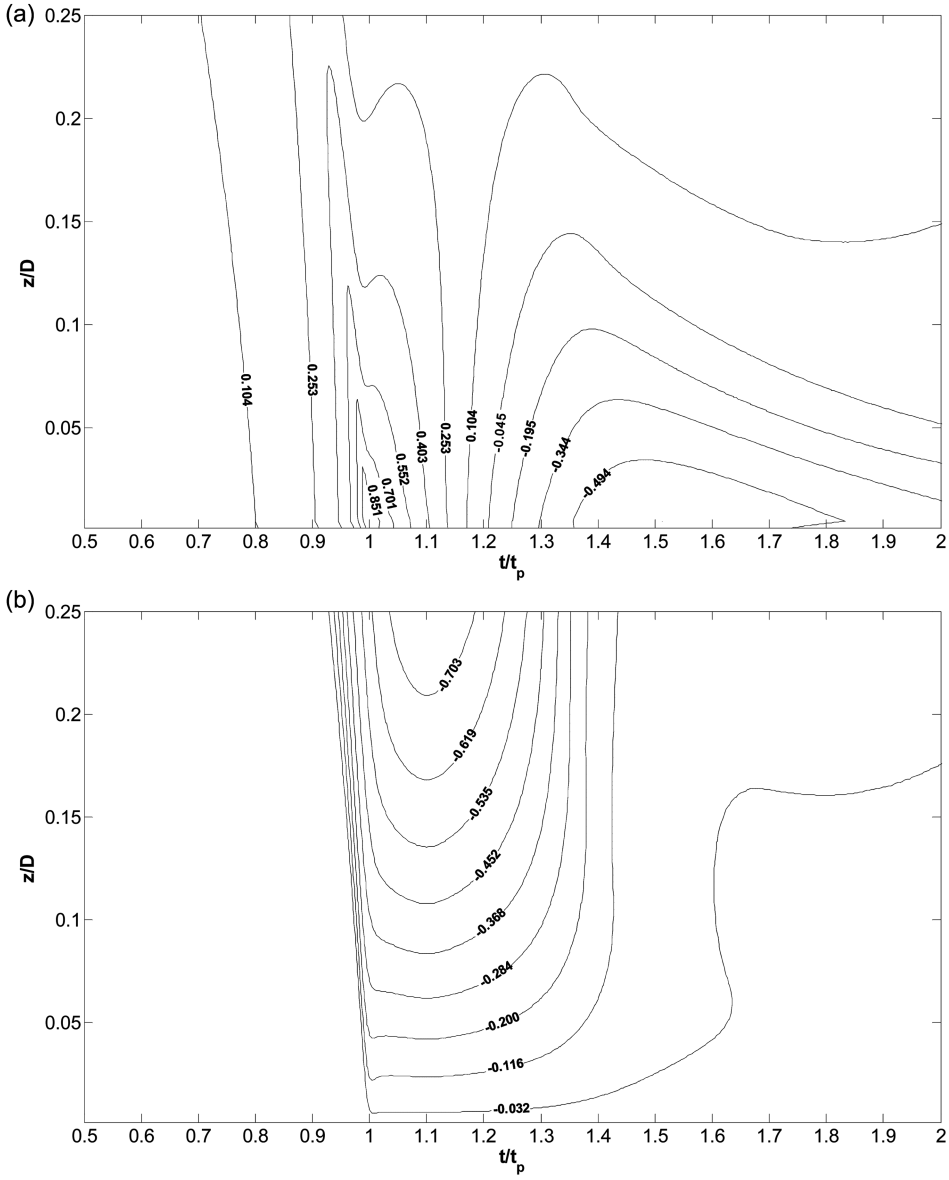

Fig. 16 Contours of (a) U/U_p and (b) W/U_p as encountered by Structure A, which moves through the CM1-Case 3 simulation domain ahead of the peak maximum gust (*N.B.* t_p is time to peak velocity)

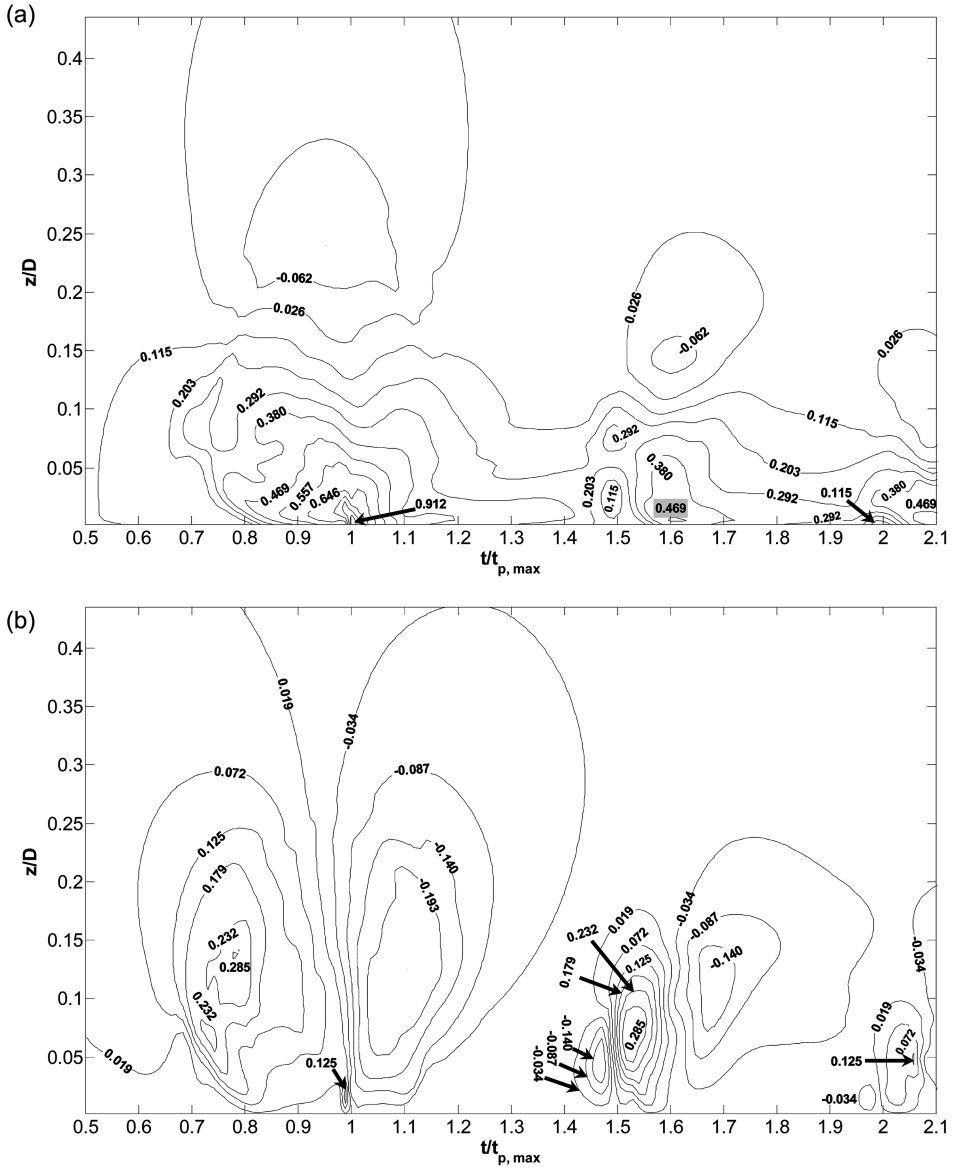

Fig. 17 Contours of (a) $U/U_{p,\max}$ and (b) $W/U_{p,\max}$ as encountered by Structure B, which experiences the peak maximum gust in CM1-Case 3 (*N.B.* $t_{p,\max}$ is time to peak maximum velocity)

with each subsequent region of rotational flow. These rotational flow regions are encountered by Structure B with a period of 0.5 to 0.6 $t_{p,\max}$ (between 0.005 and 0.004 Hz). It is worth noting that the presently-tallest guyed structure in the world (KVLY-TV mast near Blanchard, North Dakota, USA) extends to $z/D = 0.4192$.

Fig. 17(b) gives an indication that W is negligible (< 1 m/s upon closer examination of the data) at the time and location of the peak U gust ($U/U_{p,\max} = 0.912$ contour in Fig. 17(a)). However, at the timestep prior to $t_{p,\max}$, there is a fine scale flow feature near ground level. It is associated with the $W/U_{p,\max} = 0.125$ contour.

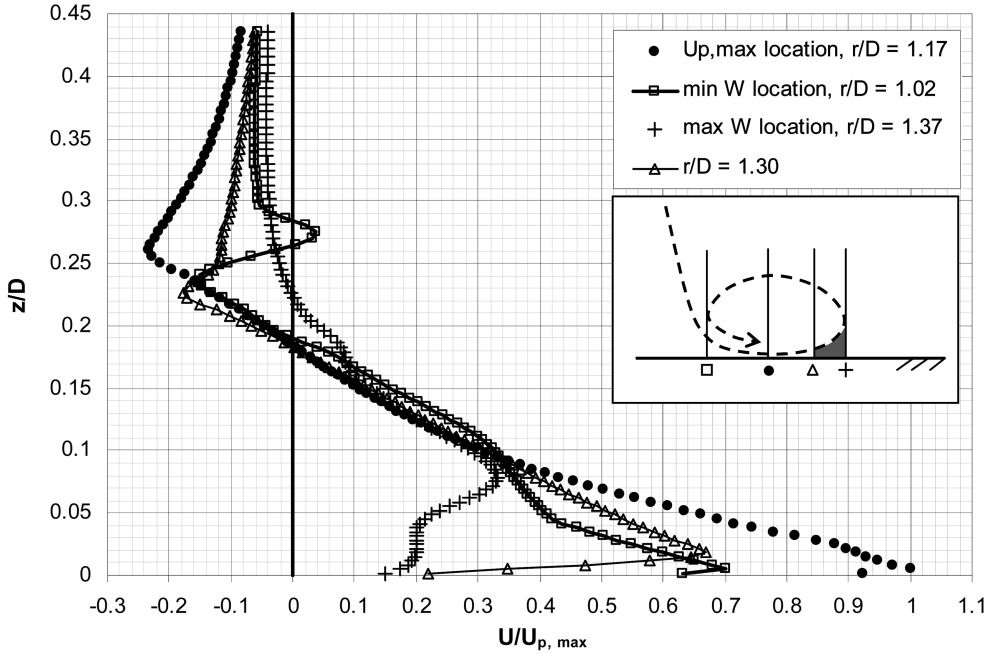

Fig. 18 Vertical profiles at different radial positions at the time of peak maximum U in CM1-Case 1

As noted in § 3a, precisely instantaneous vertical profiles are difficult to obtain in field studies. The present numerical simulations are able to provide some insight into the instantaneous profile shapes. At the instant $U_{p,\max}$ (47 m/s) occurs in CM1-Case 1, vertical profiles are plotted at the four radial locations depicted in the Fig. 18 inset. The results for CM1-Case 2 are similar to those shown in Fig. 18.

The profile shapes are clearly related to the dominant outflow vortex. Radial locations of interest correspond to the following flow features: (1) the peak maximum horizontal wind speed occurring at the middle of the horizontal extent of the dominant vortex, (2) the local vertical wind speed minimum in the trailing part of the dominant vortex, and (3) the local vertical wind speed maximum in the leading part of the dominant vortex. The only profile with a notably different shape corresponds to the third location mentioned, which is likely due to flow complexities[5] in the region beneath the elevated leading nose of the dominant vortex (shaded region in the Fig. 18 inset). Nevertheless, the U values do not exceed 10 m/s for $z/D < 0.04$ at $r/D = 1.37$. A fourth profile is plotted at an intermediate location. Fig. 19 in § 6.3 shows that the height of the profile maximum at $r/D = 1.30$ agrees well with available field data.

6.3. Comparison of velocity profiles

Fig. 19 compares the following vertical profiles:

- U/U_m from a study (Wood, *et al.* 2001) that is representative of steady, round impinging jet experiments (cf. Lin and Savory 2006, Fig. 9),
- $\langle U \rangle / \langle U \rangle_m$ from the present slot jet experiment,

[5]An adverse pressure gradient causes boundary layer separation and subsequent roll-up into secondary vortices (Alahyari and Longmire 1995).

- U/U_m from the present CM1 numerical simulations for a non-translating downburst,
- U/U_p and $U/U_{p,\max}$ from the present CM1 numerical simulation for a translating downburst,
- U/U_m from a numerical model that includes the full downdraft thermodynamics, and
- U/U_m from full-scale studies.

The largest value for each of the second, third, fifth, and sixth profiles listed above occurs within the $z/z_{0.5}$ range of 0.18 to 0.25. Between the ground and profile maximum, the CM1 non-translating downburst profiles underpredict the observed velocity profiles, whilst the slot jet velocity profile tends to exceed the observations. The translating cooling source CM1 profiles yield peak velocities at noticeably lower heights than the other profiles.

The experimental profiles represent numerous realizations, the numerical profiles are instantaneous, and the field profiles should be regarded with caution as they were extracted from radar scans where scanning time is significant. Although there is the concern that not all of these profiles are instantaneous, Fig. 19 compiles and compares results to date.

Recalling that largest horizontal velocity occurs at $z/D = 0.005$ in the present numerical simulations, Fig. 20 shows that the corresponding vertical velocity is significantly less ($U_{p,\max} = 47$ m/s in Case 1, $U_{p,\max} = 37$ m/s in Case 2, $U_p = 38$ m/s for Case 3A, and $U_{p,\max} = 69$ m/s for Case 3B). At $z/D < 0.027$ (lowest 40 m AGL), vertical speeds are less than 5 m/s. Vertical velocity is significant only at large z in the downdraft core, as seen with Case 3A. As encountered by Structure

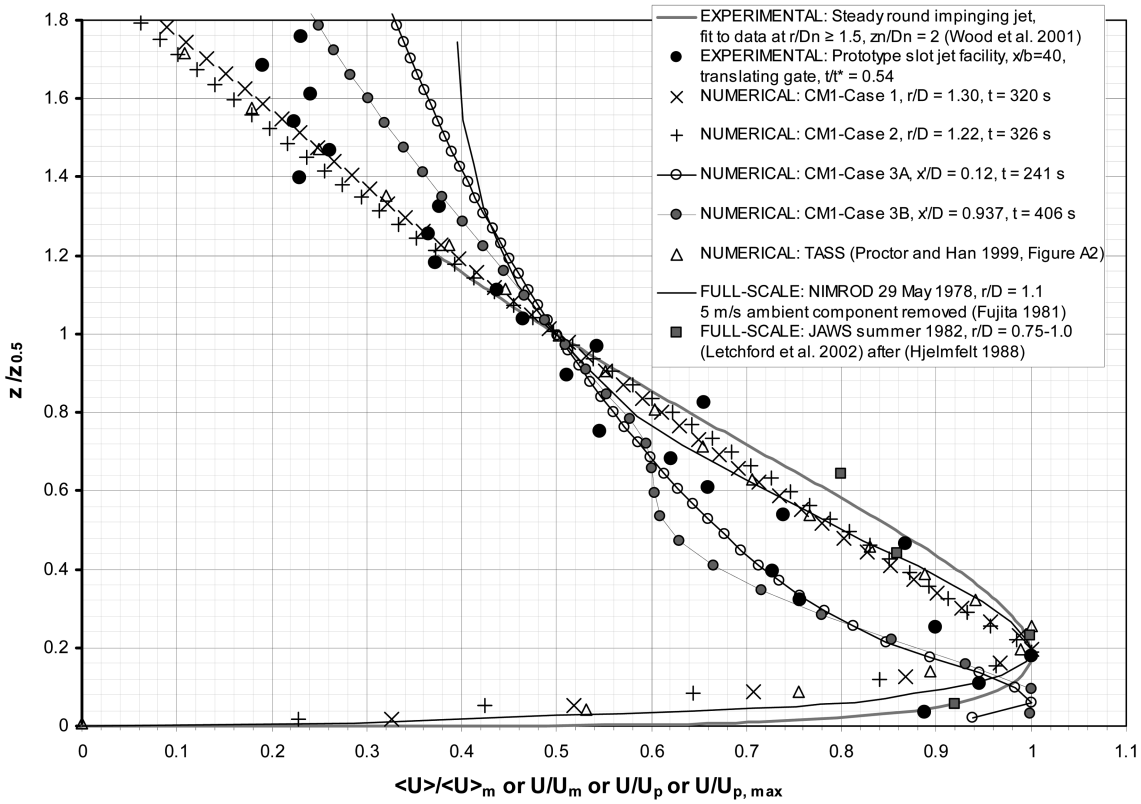

Fig. 19 Comparison of vertical profiles of horizontal velocity

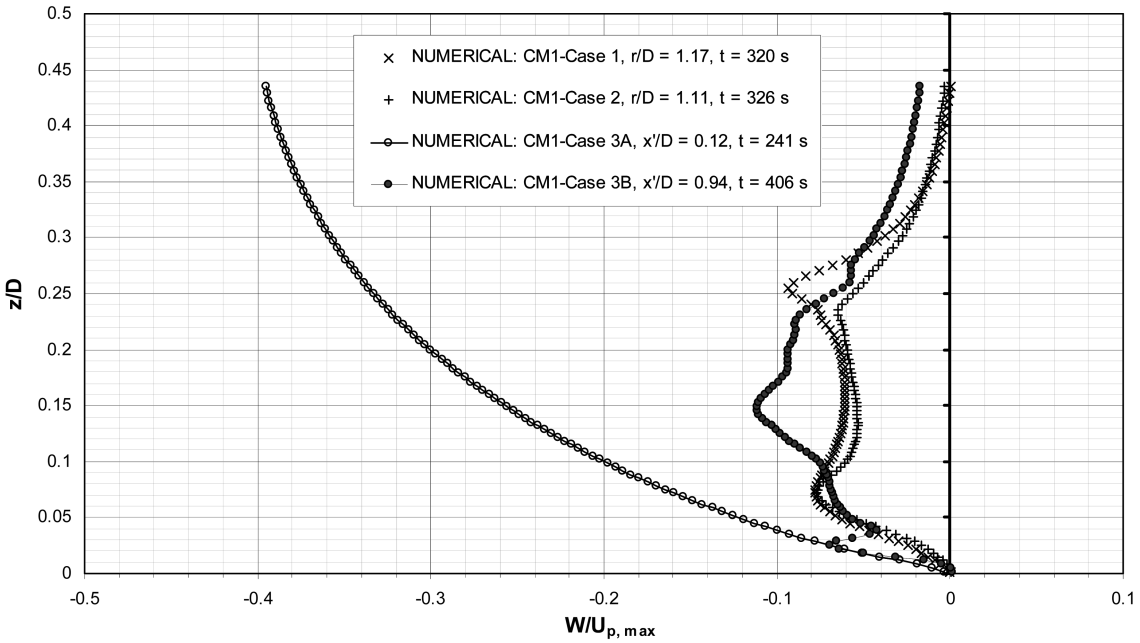

Fig. 20 Vertical profiles of vertical velocity, coinciding with $U_{p,\max}$ (or U_p for Case 3A)

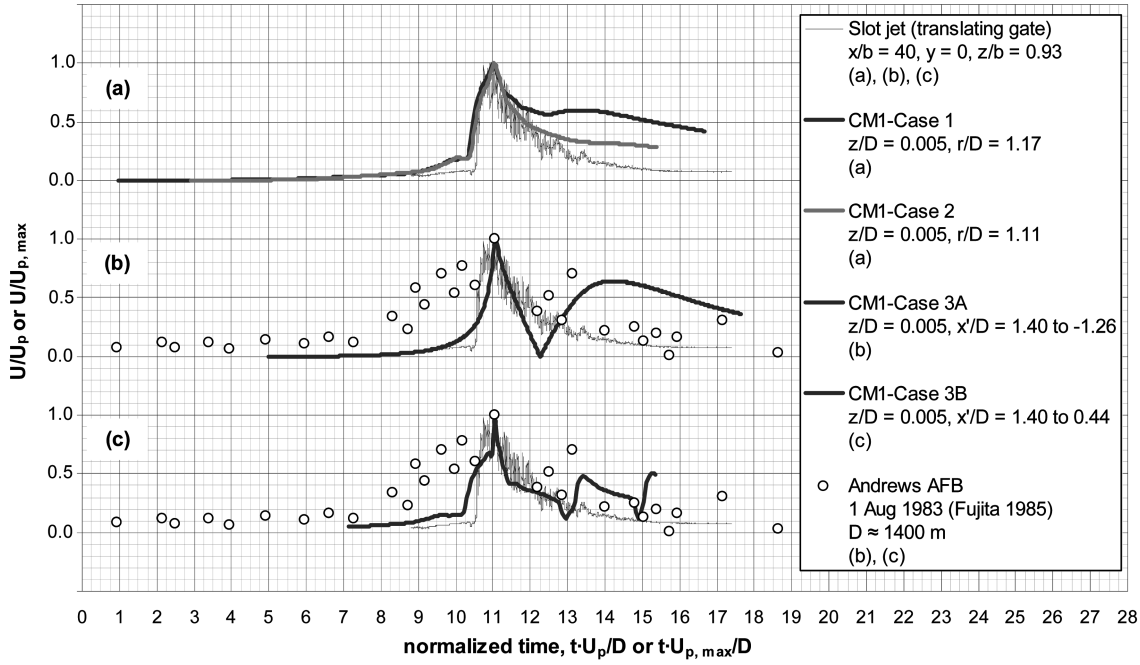

Fig. 21 Comparison of present horizontal velocity history results and a field observation

A, $W = -10$ m/s at $z = 100$ m AGL, which constitutes 48% of U at the corresponding point. At the lesser heights of typical structures (e.g. at $z = 10$ AGL), W/U is an order of magnitude smaller.

6.4. Comparison of velocity histories

Fig. 21(a) compares a translating gate slot jet history at $x/b = 40$ to Cases 1 ($U_t = 0$) and 2 ($U_t = 0$, shorter cooling forcing) from the CM1 numerical model. These histories are at the height where the largest velocity occurs in the respective vertical profiles. Time is normalized by the peak maximum (or peak) U and downdraft diameter. An effective slot jet downdraft diameter is determined based on a length scale from the numerical simulation. Dividing z where $U_{p,\max}$ occurs by D yields 7.5 m / 1500 m = 0.5%. The effective slot jet diameter is then estimated as 0.0125 m / 0.5% = 2.5 m.

After the peak maximum of the CM1-Case 1 history in Fig. 21(a), the plateau is due to the continued outflow in the wake of the dominant vortex. With a cooling forcing of shorter duration for CM1-Case 2, the computed rise and decay agree well with the measured slot jet velocity history. Figs. 21(b) and c compare a field observation with the slot jet and translating cooling source numerical simulations (Cases 3A and 3B, $U_t = 8$ m/s). The simulations appear to develop too rapidly relative to the Andrews AFB record of an extreme wet downburst outflow (Wakimoto 1985). In particular, the simulated initial rise is too sharp. However, the decay after the peak maximum in Case 3B (as encountered by the structure that experiences the 69 m/s gust) and the slot jet decay show fair agreement with the field record, given that the simulations occur under idealized conditions.

7. Scale of simulations

Table 3 summarizes the scaling achieved in various time-dependent downburst simulations. The

Table 3 Reported and estimated scales for time-dependent experiments

Study	Length scale	Velocity scale	Comments
Buoyancy-driven flow			
TASS, Proctor (1988), numerical	1:1	1:2 - 1:3	Full thermodynamics and microphysics.
Lundgren, *et al.* (1992), experimental	1:9000 - 1:45000	1:85	Release of cylindrical fluid parcel into a tank of ambient fluid of lower density.
Alahyari & Longmire (1995), experimental	1:25000	1:300	
Present cooling source / CM1 implementation, numerical	1:1	1:1	Negative buoyancy generated by increasing and then decreasing potential temperature over time, in an elevated atmospheric region.
Impinging round jet			
Kim, *et al.* (2005), numerical (FLUENT)	1:10500 - 1:52500	1:6.7	Continuous jet with impulsive start.
Mason, *et al.* (2005), experimental	1:2400 - 1:6100	1:3	Continuous jet with impulsive start.
2-D slot jet			
Present prototype facility, experimental	1:2000	1:2	Simulation of outflow region.
Expected full-size facility, experimental	1:700	1:2	Large-scale simulation of outflow region.

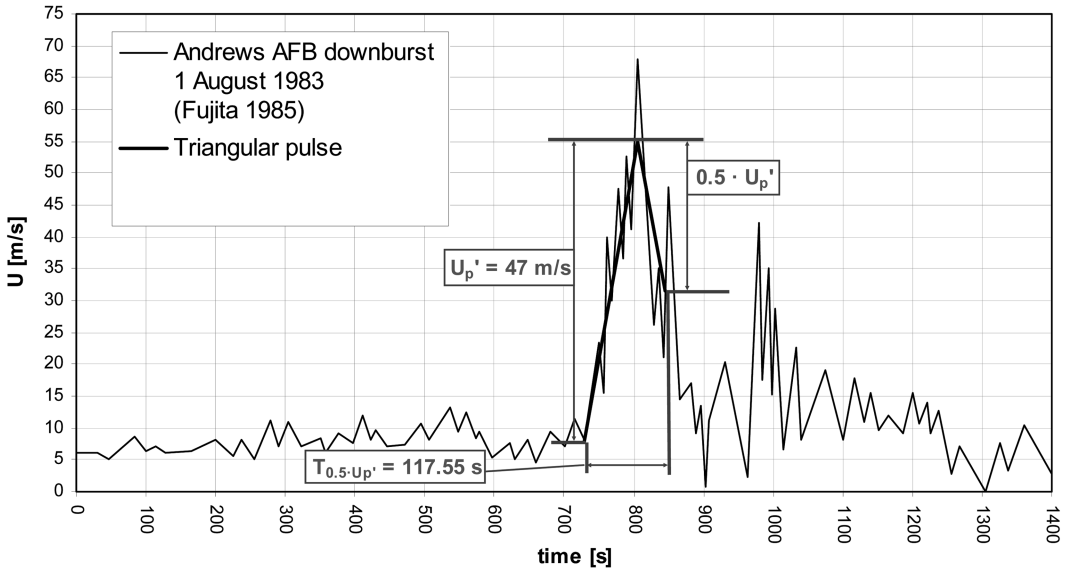

Fig. 22 Characteristic velocity and time for an observed downburst outflow

buoyancy-driven flows are the most realistic experiments since they physically model the driving mechanisms of the full-scale event. As well, they inherently simulate the transient nature of the entire downburst flow. However, the resulting outflows are extremely small in length and velocity scale. Impinging jet studies can be an order of magnitude larger, where the model scale is estimated by equating jet nozzle diameter to observed downdraft diameters. However, for impinging jet experiments, laboratory space and cost considerations become prohibitive with increasing D_n. Numerical models (e.g. TASS, WME, and CM1) have the capability to simulate events at full-scale, however, these results need to be validated with field observations or experiments.

To estimate the 2-D slot jet simulation scale, the prototype facility velocity history is compared to the history from the Andrews AFB downburst outflow. The characteristic velocity in this analysis is the peak velocity excess (U_p'). The characteristic time ($T_{0.5 \cdot Up'}$) is the total duration of the rise to U_p' and the decay to half of (U_p'). As indicated in Fig. 22, a triangular pulse (Chen and Letchford 2004) is fit to the data points to estimate these values. The length scale of the 2-D transient slot jet simulation is found with Eq. (5).

$$\frac{(U_p' \cdot T_{0.5 \cdot Up'})_{full-scale}}{(U_p' \cdot T_{0.5 \cdot Up'})_{experiment}} \tag{5}$$

It is evident from Fig. 21b that by doubling $T_{0.5 \cdot Up'}$ of the prototype facility, a better match with the full-scale history would be achieved. As listed in Table 3, the achievable length scale with the full-size downburst outflow simulator is estimated to be significantly larger than in previous work. The velocity scale is based on the simulated peak velocity and that observed in the Andrews AFB event.

8. Conclusions

The difficulty of downburst field observation has motivated substantial efforts towards physical and numerical simulation. Previous simulations have advanced our understanding of the temporal

evolution of the downburst flow field. The logical extension of this knowledge is to apply it to the engineering of structures that are subjected to this type of intense wind. Previous approaches to physical modelling do not produce outflows of sufficiently large scale to study the wind loading on common structures. With the addition of an actuated slot in a conventional atmospheric boundary layer wind tunnel, the length scale of the simulated time-dependent outflow is sufficiently increased to facilitate studies with structural models.

The Andrews AFB downburst velocity record suggests that the outflow wind direction is fairly constant during the leading side velocity peak. As such, a slot jet approach is applicable for modelling the outflow over the duration that the event attains its highest intensity. A slot jet facility is a practical and realizable approach towards simulating the near-surface peak gust. A translating gate design generates velocity profiles and histories that are comparable to available full-scale data. The present results suggest that the duration of the gate actuation opening phase should be lengthened from the values used in the present study.

Details of the outflow at peak maximum intensity are particularly useful for wind engineering purposes. By implementing the Bryan Cloud Model (CM1) with a cooling source approach, damaging outflows are modelled at high spatial and temporal resolution, whilst retaining a good approximation of the true flow dynamics. The ease of modifying the cooling forcing makes it a useful engineering tool for studying the outflow region of isolated downbursts. With respect to the peak maximum horizontal outflow velocity from a non-translating downburst, the present numerical model predicts that the shape of the vertical profile of U resembles a wall jet profile with a pronounced maximum. The instantaneous vertical velocity component corresponding to the peak maximum U is found to be relatively insignificant. In addition to its increased magnitude, the peak maximum U in a translating downburst occurs closer to the surface than that in a non-translating event.

A steady outflow profile generally has a fuller shape than the peak maximum profiles from time-dependent simulations. With respect to profile shape and height where the largest velocity value occurs, steady flow simulations appear to adequately represent outflows from non-translating downbursts. However, the computed translating downburst outflow exhibits a strong periodicity, which would be neglected in steady simulations.

The present article addresses outflows from isolated downbursts. Available field observations suggest that the present discussion may be extended to larger convective downdraft phenomena, such as rear-flank downdrafts. Since RFDs exhibit dynamic behaviour and occur as a constituent of complex thunderstorm flows, further investigation is required to determine whether the basic approaches discussed herein may serve as building blocks for advanced simulations.

Acknowledgements

Manitoba Hydro, Natural Sciences and Engineering Research Council of Canada, and the Institute for Catastrophic Loss Reduction provided financial support for this work. The UWO University Machine Shop fabricated parts for the experimental facility. Some of the test equipment was kindly made available by Dr. G.A. Kopp and Dr. R.J. Martinuzzi. Dr. J.D. Holmes provided helpful feedback and insight.

References

Alahyari, A. A. (1995), “Dynamics of laboratory simulated microbursts”, University of Minnesota, PhD thesis,

December.
Alahyari, A. and Longmire, E. K. (1995), "Dynamics of experimentally simulated microbursts", *AIAA J.*, **33**(11), 2128-2136.
Arakawa, A. and Lamb, V. R. (1977), "Computational design of the basic dynamical processes of the UCLA general circulation model", *Methods in Computational Physics*, editor: J. Chang, Academic Press, New York, NY, USA, **17**, 173–265.
Bakke, P. (1957), "An experimental investigation of a wall jet", *J. Fluid Mech.*, **2**, 467-472.
Bryan, G. H. and Fritsch, J.M. (2002), "A benchmark simulation for moist nonhydrostatic numerical models", *Mon. Wea. Rev.*, **130**(12), 2917-2928.
Caracena, F. (1982), "Is the microburst a large vortex ring imbedded in a thunderstorm downdraft?", *EOS Transactions of the American Geophysical Union*, **63**, 899.
Charba, J. (1974), "Application of gravity current model to analysis of squall-line gust front", *Mon. Wea. Rev.*, **102**(2), 140-156.
Chay, M. T. and Letchford, C. W. (2002), "Pressure distributions on a cube in a simulated thunderstorm downburst – Part A: stationary downburst observations", *J. Wind Eng. Ind. Aerodyn.*, **90**, 711-732.
Chen, L. and Letchford, C. W. (2004), "A deterministic-stochastic hybrid model of downbursts and its impact on a cantilevered structure", *Eng. Struct.*, **26**, 619-629.
Chen, L. and Letchford, C. W. (2005), "Proper orthogonal decomposition of two vertical profiles of full-scale nonstationary downburst wind speeds", *J. Wind Eng. Ind. Aerodyn.*, **93**, 187-216.
Chen, L. and Letchford, C. W. (2006), "Multi-scale correlation analyses of two lateral profiles of full-scale downburst wind speeds", *J. Wind Eng. Ind. Aerodyn.*, **94**, 675-696.
Choi, E. C. C. and Hidayat, F. A. (2002), "Dynamic response of structures to thunderstorm winds", *Prog. Struct. Eng. Mater.*, **4**, 408-416.
Doviak, R. J. and Zrnić, D. S. (1988), "The Doppler weather radar", in *Aspects of Modern Radar*, editor: E. Brookner, Artech House, Norwood, MA, USA, 487-561.
Droegemeier, K. K. and Wilhelmson, R. B. (1987), "Numerical simulation of thunderstorm outflow dynamics. Part I: Outflow sensitivity experiments and turbulence dynamics", *J. Atmos. Sci.*, **44**(8), 1180-1210.
Fujita, T. T. (1981), "Tornadoes and downbursts in the context of generalized planetary scales", *J. Atmos. Sci.*, **38**(8), 1511-1534.
Fujita, T. T. (1983), "Andrews AFB microburst", University of Chicago, Department of Geophysical Sciences, Satellite and Mesometeorology Research Project, Research Paper #205, 38 pp.
Fujita, T. T. (1985), "The downburst: microburst and macroburst", University of Chicago, Department of Geophysical Sciences, Satellite and Mesometeorology Research Project, Research Paper #210, 128 pp.
Gast, K. D. and Schroeder, J. L. (2003), "Supercell rear-flank downdraft as sampled in the 2002 Thunderstorm Outflow Experiment", *Proceedings of the 11th International Conference on Wind Engineering*, Lubbock, TX, USA, 2-5 June, 2233-2240.
Gast, K. D. and Schroeder, J. L. (2004), "Extreme wind events observed in the 2002 Thunderstorm Outflow Experiment", *22nd Conference on Severe Local Storms*, Hyannis, MA, USA, 4-8 October, Paper 7A.6.
Goff, R. C. (1976), "Vertical structure of thunderstorm outflows", *Mon. Wea. Rev.*, **104**(11), 1429-1440.
Hjelmfelt, M.R. (1988), "Structure and life cycle of microburst outflows observed in Colorado", *J. Appl. Meteor.*, **27**(8), 900-927.
Holmes, J. D. and Hangan, H. M. (2006), "Some engineering aspects of convective downdrafts", The Boundary Layer Wind Tunnel Laboratory, The University of Western Ontario, BLWT-2-2006, July.
Holmes, J. D. and Oliver, S. E. (2000), "An empirical model of a downburst", *Eng. Struct.*, **22**, 1167-1172.
Jørgensen, F.E. (2005), "How to measure turbulence with hot-wire anemometers – a practical guide", Dantec Dynamics A/S publication no. 9040U6154, Skovlunde, Denmark.
Kim, J., Ho, T. C. E. and Hangan, H. (2005), "Downburst induced dynamic responses of a tall building", *Proceedings of the 10th Americas Conference on Wind Engineering*, Baton Rouge, USA, 31 May-4 June, CD-ROM.
Klemp, J. B. and Wilhelmson, R. B. (1978), "The simulation of three-dimensional convective storm dynamics", *J. Atmos. Sci.*, **35**(6), 1070-1096.
Letchford, C. W. and Chay, M. T. (2002), "Pressure distributions on a cube in a simulated thunderstorm downburst-Part B: moving downburst observations", *J. Wind Eng. Ind. Aerodyn.*, **90**, 733-753.
Letchford, C. W., Mans, C. and Chay, M. T. (2002), "Thunderstorms – their importance in wind engineering (a

case for the next generation wind tunnel)", *J. Wind Eng. Ind. Aerodyn.*, **90**(12-15), 1415-1433.
Lin, W. E. and Savory, E. (2006), "Large-scale quasi-steady modelling of a downburst outflow using a slot jet", *Wind Struct.*, **9**(6), 419-440.
Linden, P. F. and Simpson, J. E. (1985), "Microbursts: a hazard for aircraft", *Nature*, **317**, 601-602.
Linden, P. F. and Simpson, J. E. (1986), "Gravity-driven flows in a turbulent fluid", *J. Fluid Mech.*, **172**, 481-497.
Lundgren, T. S., Yao, J. and Mansour, N. N. (1992), "Microburst modelling and scaling", *J. Fluid Mech.*, **239**, 461-488.
Mason, M., Letchford, C. W. and James, D. (2003), "Pulsed jet simulation of a thunderstorm downburst", *Proceedings of the 11th International Conference on Wind Engineering*, Lubbock, TX, USA, 2-5 June, 2249-2256.
Mason, M. S., Letchford, C. W. and James, D. L. (2005), "Pulsed wall jet simulation of a stationary thunderstorm downburst, Part A: Physical structure and flow field characterization", *J. Wind Eng. Ind. Aerodyn.*, **93**, 557-580.
McNulty, R. P. (1991), "Downbursts from innocuous clouds: an example", *Wea. Forecasting*, **6**(1), 148-154.
Orf, L. G. and Anderson, J. R. (1999), "A numerical study of traveling microbursts", *Mon. Wea. Rev.*, **127**(6), 1244-1258.
Orf, L. G., Anderson, J. R. and Straka, J. M. (1996), "A three-dimensional numerical analysis of colliding microburst outflow dynamics", *J. Atmos. Sci.*, **53**(17), 2490-2511.
Proctor, F. H. (1988), "Numerical simulations of an isolated microburst. Part I: dynamics and structure", *J. Atmos. Sci.*, **45**(21), 3137-3160.
Proctor, F. H. (1989), "Numerical simulations of an isolated microburst. Part II: sensitivity experiments", *J. Atmos. Sci.*, **46**(14), 2143-2165.
Proctor F. H. and Han J. (1999), "Numerical study of wake vortex interaction with the ground using the Terminal Area Simulation System", *37th Aerospace Sciences Meeting & Exhibit*, Reno, NV, USA, 11-14 January, AIAA-99-0754.
Schlichting, H. (1979), *Boundary-layer Theory*, 7th edition, McGraw-Hill, New York, NY, USA.
Selvam, R. P. and Holmes, J. D. (1992), "Numerical simulation of thunderstorm downdrafts", *J. Wind Eng. Ind. Aerodyn.*, **41-44**, 2817-2825.
Stull, R. B. (1988), *An Introduction to Boundary Layer Meteorology*, Kluwer Academic Publishers, Boston, MA, USA.
Stull, R. B. (1995), *Meteorology Today for Scientists and Engineers: A Technical Companion Book,* West Publishing Company, St. Paul, MN, USA.
Verhoff, A. (1970), "Steady and pulsating two-dimensional turbulent wall jets in a uniform stream", Princeton University, PhD thesis.
Wakimoto, R. M. (1985), "Forecasting dry microburst activity over the High Plains", *Mon. Wea. Rev.,* **113**(7), 1131-1143.
Wakimoto, R. M. (2001), "Convectively driven high wind events", *Severe Convective Storms, Meteor. Monogr.*, editor: C.A. Doswell III, publisher: American Meteorological Society, **28**(50), 255-298.
Wood, G. S., Kwok, K. C. S., Motteram, N. A. and Fletcher, D. F. (2001), "Physical and numerical modelling of thunderstorm downbursts", *J. Wind Eng. Ind. Aerodyn.*, **89**, 535-552.
Xu, Z. (2004), "Experimental and analytical modeling of high intensity winds", The University of Western Ontario, PhD thesis, December.
Yao, J. and Lundgren, T. S. (1996), "Experimental investigation of microbursts", *Exp. Fluids*, **21**, 17-25.

Nomenclature

b	slot height
g	gravitational acceleration
k	turbulent kinetic energy
m(subscript)	largest value in space
n	number of realizations
nt	time step index (CM1)
p(subscript)	largest value in time
r	radial direction (axisymmetric flow)

s	ordered sample number
x	streamwise direction (slot jet)
x'	horizontal distance from geometric centre of cooling source volume (CM1)
y	spanwise direction (slot jet)
t	time
t_p	time to peak velocity with respect to the simulation start time (CM1)
$t_{p,\,\max}$	time to peak maximum velocity w.r.t. the simulation start time (CM1)
t_s	time corresponding to ordered sample number s
t^*	total duration to open and close gate
w_1, w_2, w_3	moving average weights
z	vertical direction
z_{axis}	height of vortex axis above solid boundary
z_n	nozzle or cylinder exit height above impingement plane
z_0	aerodynamic roughness length
$z_{0.5}$	vertical half-width (where $U = 0.5 \cdot U_m$ above the location of U_m)
A(subscript)	Structure A (CM1)
B(subscript)	Structure B (CM1)
C_{DN}	drag coefficient for statically neutral environmental conditions
D	downdraft diameter
D_n	nozzle or cylinder exit diameter
$\hat{I}_u$	estimated effective turbulence intensity
N	number of measurement locations in a profile
R_0	length scale (released fluid)
Re_n	nozzle Reynolds number (impinging jet)
Re_ρ	flow Reynolds number (released fluid)
T_0	time scale (released fluid)
$T_{0.5 \cdot Up'}$	velocity history time scale
U	horizontal velocity
U_j	slot exit velocity
$U_{j,\,steady}$	steady slot exit velocity
U_m	maximum velocity: largest value in space (typically pertaining to a vertical profile at fixed r or x)
U_t	downburst translational velocity
U_p	peak velocity: largest value in time
$U_{p,\,\max}$	peak maximum velocity: largest overall value in an unsteady flow field
U_p'	peak velocity excess above baseline velocity
U_{MA}	moving average of U history
$<U>$	ensemble-averaged velocity
V_0	velocity scale (released fluid)
W	vertical velocity
$W_{\min}$	minimum vertical velocity
W_n	nozzle exit velocity (impinging jet)
Y	working section span (slot jet)
ε	dissipation rate of turbulent kinetic energy
$\Delta\theta$	change in angular position (rotating gate)
ν	kinematic viscosity
ρ	fluid density
$\Delta\rho$	fluid density difference